nuclear fusion
IAEA

PAPER • OPEN ACCESS

SOLPS-ITER simulation of W limiter start-up on ITER

To cite this article: Y. Zhang *et al* 2025 *Nucl. Fusion* **65** 056035

OPEN ACCESS
IOP Publishing | International Atomic Energy Agency
Nuclear Fusion
Nucl. Fusion **65** (2025) 056035 (22pp)
https://doi.org/10.1088/1741-4326/adcd85

SOLPS-ITER simulation of W limiter start-up on ITER

Y. Zhang[1], A.A. Pshenov[2], R.A. Pitts[2], X. Bonnin[2], M. Dubrov[2], Y. Gribov[2], A. Kirschner[3], C. Baumann[3], S. Brezinsek[3], J. Romazanov[3], Chaofeng Sang[1,*] and Dezhen Wang[1]

[1] Key Laboratory of Materials Modification by Laser, Ion and Electron Beams (Ministry of Education), School of Physics, Dalian University of Technology, Dalian 116024, China
[2] ITER Organization, Route de Vinon-sur-Verdon, CS 90 046, 13067 St Paul Lez Durance Cedex, France
[3] Forschungszentrum Jülich GmbH, Institute of Fusion Energy and Nuclear Waste Management—Plasma Physics, 52425 Jülich, Germany

E-mail: sang@dlut.edu.cn

Received 26 December 2024, revised 18 March 2025
Accepted for publication 16 April 2025
Published 25 April 2025

Abstract

The switch from beryllium (Be) to tungsten (W) first wall (FW) armor in the new ITER baseline Pitts *et al* (2025 *Nucl. Mater. Energy* **42** 101854), Loarte (n.d. *Plasma Phys. Control. Fusion*) will impact the limiter start-up phase due to the much higher radiated power associated with W impurity. To assess this impact, a large database of SOLPS-ITER simulations of the hydrogen (H) plasmas in contact with the tungsten (W) limiter has been constituted, including transport of all individual W charge states up to a given cut-off. It has been shown that the plasma-limiter system exhibits strong self-regulating properties due to the strong dependence of W self-sputtering on the electron temperature at the last closed flux surface (LCFS). This self-regulation limits the power (P_{LCFS}) crossing the LCFS into the scrape-off layer (SOL), resulting in high core radiated fractions (f_{rad}), but at the same time reducing the FW heat loads. Regression within the database also permits the derivation of a simple scaling relationship between the plasma temperature and density at the LCFS and the heating power which is used to construct a boundary condition for time-dependent scenario simulations. Simulations of W prompt redeposition using the ERO code for selected plasma backgrounds in the database found that 25%–45% of the eroded W particles reside in plasma for less than a gyration time. The reverse effect of the prompt redeposition on the background solution, assessed by re-running SOLPS-ITER with reduced W sputtering yield, proved have a greater effect on the solution than the impact of SOL plasma transport variation. Self-consistent simulations with an appropriate prompt redeposition model are therefore required to improve the prediction for ITER and to validate the code against W limiter start-up experiments on current devices. To assess the consequence of the inevitable background impurities present in real tokamak start-up plasmas, some preliminary simulations have also been performed with feedback-controlled nitrogen (N) seeding. It is found that even moderate N content leads to saturation of P_{LCFS}, and hence f_{rad}, with respect to plasma density variation. The plasma density increase with seeding leads to

* Author to whom any correspondence should be addressed.

redistribution of radiation between the W and N, preferentially cooling the edge in comparison with pure plasmas.

Keywords: SOLPS-ITER, tungsten limiter, plasma start-up, ITER

(Some figures may appear in colour only in the online journal)

1. Introduction

Since 2023, the ITER Organization has been undergoing a process of re-baselining, a key element of which is the exchange of first wall (FW) material from beryllium (Be) to tungsten (W) [1, 2]. This change offers numerous benefits, including a decrease in FW erosion, which subsequently reduces the tritium (T) fuel retention in Be co-deposits, a reduction in associated dust production and higher resilience of the FW to fast transient thermal loads. It also simplifies the assembly/disassembly process since Be handling is no longer required, and allows for earlier testing of reactor relevant FW materials. This exchange of FW material is not, however, without risk: the core plasma is orders of magnitude more resilient to contamination by Be than W and the extremely beneficial gettering action of Be for oxygen (O) is lost, making plasma start-up potentially much more difficult [1]. It is this start-up issue which is the focus of the present study which concerns new plasma boundary simulations of the ITER current ramp-up phase in limiter configuration, expanding significantly on the preliminary outcome of this work reported in [1].

In ITER, plasma current ramp-up is foreseen on the inboard, high field side of the torus [3]. Unlike in most current devices, where this ramp-up in limiter configuration typically occurs in $\geqslant$1 s, in ITER this phase lasts $\sim$10 s. Impurities released (primarily by physical sputtering) in limiter configurations have a high probability of crossing the last closed flux surface (LCFS) and hence directly contaminating the confined plasma. Whereas for Be such core assimilation is of little consequence for the limiter plasma, in the case of W, radiative collapse during the current ramp is a real concern [3].

This concern stimulated a joint effort of SOLPS-ITER, DINA and JINTRAC code simulations of ITER start-up in limiter configuration, each focusing on distinct aspects of the issue. The first results of this program were reported in [1], demonstrating in particular that in the absence of additional impurities, the plasma-limiter system is governed by W self-sputtering and exhibits strong self-regulating properties, driving the system to a state where the average W self-sputtering yield over the limiter surface converges toward unity.

To support the assessments in [1], a provisional database of stationary (thus time independent) simulations with the SOLPS-ITER code [4] was constituted for limiter plasmas at a fixed magnetic equilibrium corresponding to one representative time instant in a typical ITER ramp-up scenario designed with the DINA code [5]. Scans of input power and density in these simulations (in which W release and transport was fully included) enabled the derivation of boundary conditions that, in turn, were used by DINA to assess the whole limiter start-up scenario, from plasma breakdown to X-point formation [6]. These DINA simulations exhibited that, if the O level is sufficiently low and the electron-cyclotron (EC) heating waveform is sufficiently smooth (i.e. the heating power gradually increases to avoid triggering excessive W sputtering due to momentary sharp rises of the edge plasma temperature), the limiter phase can be successfully navigated.

In this paper, the provisional SOLPS-ITER W limiter simulation database is significantly expanded and improved to include a number of physics elements acknowledged as clearly lacking in the treatment of [1]. Key such aspects are the impact of W prompt re-deposition, the influence of residual or seeded impurities and sensitivity to the radial plasma transport profiles in the scrape-off layer (SOL). Section 2 describes the self-regulation mechanism governing the behavior of the limiter plasma in interaction with a W surface. Section 3 introduces the computational setup for the SOLPS-ITER simulations, including key assumptions such as boundary conditions at the sheath interface, the rationale for the chosen width of the computational grid, and the number of W charge states followed in the simulations. Section 4 presents the expanded database of limiter simulations covering different SOL transport assumptions and heating power levels and compares them to the initial database described in [1]. Sections 5 and 6 describe the more advanced simulations with which the role of 'prompt redeposition' of the eroded W and the system's response to residual or seeded impurities are studied. A summary and conclusions are given in section 7.

2. Self-regulation of the 'plasma–W limiter' system

We first explore the general properties of a pure hydrogen (H) plasma in contact with a W limiter and establish some theoretical expectations regarding this system behavior. This will later be validated using the sophisticated 2D SOLPS-ITER simulations in which W is self-consistently evolved and transported. In what follows, we analyze a stationary limiter plasma (as schematically illustrated in figure 1) which remains in contact with a W surface for several particle confinement times, allowing eroded W to penetrate into the core and reach an equilibrium state. This system is strongly governed by the W self-sputtering.

If the volume averaged core W concentration, $<c_W>$ is negligible so that W does not contribute significantly to radiation, the plasma temperature at the LCFS, $T_{e,LCFS}$ will easily reach several hundred eV even at rather modest heating power (P_{heat}). Under such conditions, the SOL plasma is non-dissipative so that the temperature at the sheath interface is

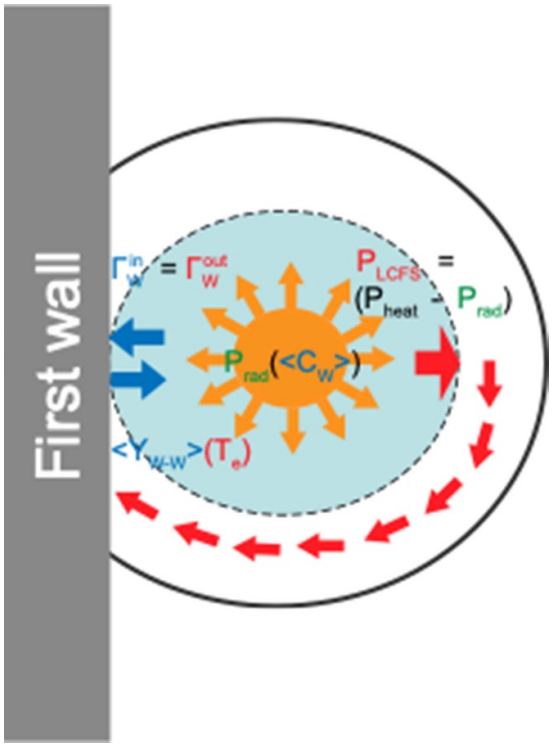

Figure 1. Schematic drawing of a limiter plasma in contact with a W FW surface, illustrating the self-regulation mechanism introduced by the strong W self-sputtering dependence on plasma temperature at the limiter.

almost identical to that upstream. As a result, H ions are accelerated by the sheath potential to energies above the W sputtering threshold, thereby generating an initial W seed. As soon as the first W atoms are eroded and ionized, they initiate an avalanche-like self-sputtering process due to their high mass and very high sheath acceleration at these temperatures (in turn due to the relatively high charge states that can be reached for W ions returning to the limiter). Since the limiter SOL plasma has a relatively low density and the contact with the limiter surface is close to the LCFS, a large fraction (typically $\sim$ 30%–50%) of the eroded W penetrates into the core. As a consequence, $<c_W>$ in the core rises rapidly, intensifying the core plasma radiation losses, P_{rad}. This in turn leads to a reduction of the power entering the SOL across the LCFS, $P_{LCFS} = P_{heat} - P_{rad}$. Reduced P_{LCFS} drives T_e down in the limiter contact area, in turn lowering W erosion. If the increase in P_{rad} is sufficient that the average self-sputtering yield of tungsten falls below unity ($<Y_{W-W}> <1$), the W core source reduces, driving $<c_W>$ and P_{rad} down and P_{LCFS} increases again. This simple feedback loop forms a strong connection between $P_{LCFS,}$ governing the W erosion, and $<c_W>$ governing the radiation losses, driving the system toward a solution corresponding to $<Y_{W-W}> = 1$ at the limiter surface.

Using this simple framework, we can now roughly estimate the level of P_{LCFS} required to maintain the system in such an equilibrium state. Taking the sheath acceleration into account and assuming that electron and ion temperatures in the limiter contact area are roughly equal, $T_e = T_i = T$, the average energy of impinging W ions in H background plasmas may be evaluated as $E_W = 2.5 \times T \times <Z_W>(T) + 2 \times T$ [7], where $<Z_W>(T)$ is the average charge of the impinging W ions. Since the limiter SOL plasma density is relatively low, $<Z_W>(T)$ can be estimated using coronal equilibrium [8]. For simplicity, we assume that W ions impact the surface orthogonally, though this is largely satisfied given that the trajectories of relatively highly charged heavy ions are significantly straightened by the sheath acceleration [9]. Using the Eckstein formula for W self-sputtering [10], fitted to the data from [11] the equilibrium value of T providing $Y_{W\text{-}W}(T) = 1$ is about 36 eV (see figure 2) and corresponding $<Z_W>(T)$ is approximately 9. It is worth noting that using more recent sputtering data from [12] results in a noticeably higher equilibrium values of $T \approx 48$ eV and $<Z_W>(T) \approx 11$. Nevertheless, in what follows, we use the sputtering data from [11] because it is implemented in the current EIRENE code version (EIRENE handles the neutral kinetics and wall interactions inside the SOLPS package). This value of T is insufficient to accelerate the H ions to energies above the H $\rightarrow$ W sputtering threshold, confirming that, despite the fact that the H ion flux to the limiter surface is several orders of magnitude higher than that of W, its impact on the steady-state erosion process is negligible. Nevertheless, it plays a crucial role in starting the avalanche process, along with the residual impurities present in the limiter plasma after the break-down.

It is now possible to estimate the level of P_{LCFS} required to sustain the equilibrium SOL solution. This cannot be done in general form as outlined above since device-specific input parameters are required. We use the parameters corresponding to a particular time instant during a standard ITER limiter current ramp-up scenario with plasma current $I_p = 2$ MA (described in detail in the next section). The target density for this plasma corresponds to a Greenwald fraction of $<n_e>/n_{GW} \sim 50\%$ [6], so we assume (quite arbitrarily) that the plasma density at the LCFS is around 30% of n_{GW}, i.e. $n_{e,LCFS}$ (10^{20} m^{-3}) = 0.3 $\times$ I_p (MA)/($\pi \times a^2$ (m)), where a is the minor radius of the plasma column ($\sim$ 2 m in this ITER case). For the plasma in question this gives $n_{e,LCFS} \sim 5 \times 10^{18}$ m^{-3}. Since typically $<c_W> \sim 10^{-4}$, its contribution to n_e can be neglected and for simplicity in the estimates we assume $n_{e,LCFS} = n_{H+,LCFS} = n_{LCFS}$. Now, assuming a simple dissipation-free isothermal SOL, the parallel power flux to the target surface can be written as [7]:

$$q_{||} = \gamma \times n_{LCFS} \times c_s \times T_{LCFS}/2, \qquad (1)$$

where γ is the heat transmission factor and c_s is the plasma sound speed. Adopting the standard value of $\gamma \sim 8$ [7], $q_{||} \sim 5$ MW m^{-2} for a H plasma. Finally, relating P_{LCFS} to $q_{||}$ through simple zero-dimensional power balance in the usual way [7]:

$$P_{LCFS} = 4 \times \pi \times q_{||} \times \lambda_q \times R_{OMP} \times (B_p/B), \qquad (2)$$

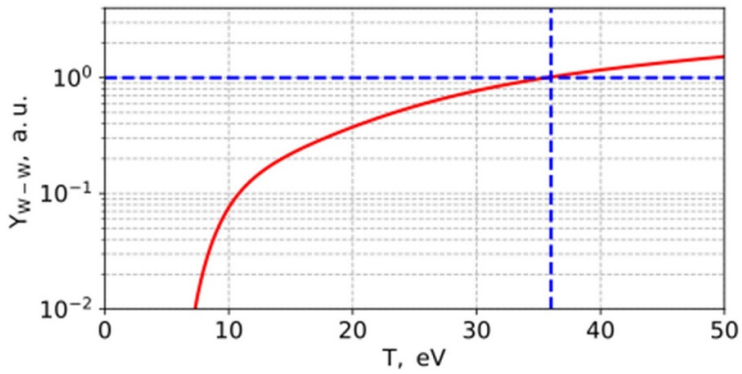

Figure 2. Tungsten self-sputtering yield ($Y_{W\text{-}W}$) as a function of the plasma temperature (assuming $T_e = T_i = T$) at the sheath entrance, assuming impinging ion energy $E_W = 2.5 \times T \times <Z_W>(T) + 2 \times T$, where $<Z_W>(T)$ is the average ion charge corresponding to 'coronal equilibrium' conditions.

where R_{OMP} is a radius of the plasma at the outer midplane (OMP), B and B_p are the total and poloidal magnetic field strengths, respectively, and λ_q is the exponential decay length of the heat flux at OMP. For our ITER case, $R_{OMP} \approx R + a$, where $R = 6$ m and $a = 2$ m are major and minor radii of the plasma, and $B_p/B = 0.045$. Obtaining a proper estimate for λ_q in these conditions can be problematic as will be discussed later. For this simple estimate we use a narrow λ_q channel width of 4 mm, found by regression from the multi-tokamak database used previously to guide the ITER FW panel shaping [13]. Introducing these values into equation (2) gives $P_{LCFS} \sim 0.85$ MW.

Therefore, in this simplified physical picture, as long as P_{heat} exceeds the equilibrium P_{LCFS} (which scales linearly with n_{LCFS}), the equilibrium T_{LCFS} remains virtually unchanged. The difference between P_{heat} and the equilibrium $P_{LCFS}(n_{LCFS})$ is radiated in the core by the accumulated W impurity. This requirement, along with the core transport profiles, in turn governs the resulting $<c_W>$ inside the confined region.

However, the real-world situation is more complex. A number of effects which are not included in this 'toy' model can only be accounted for by numerical simulations with edge transport codes (in our case SOLPS-ITER):

- Density, temperature, and particle fluxes at the limiter surface are not uniform but have different profiles and the resulting peak of erosion is shifted away from the tangency point;
- The electron and ion temperatures are not equal and are not the only factor determining $<Y_{W\text{-}W}>$; the angular distribution and the coupling of the higher W charge-states to the main plasma flow will also impact the impinging energy;
- The W distribution across charge states deviates from the coronal approximation, since some of the W ions originate from ionization in the SOL, while others reside in the confined region, where temperatures are higher, without a chance to recombine on the way to the limiter;
- So-called 'prompt redeposition' [14] will effectively reduce $<Y_{W\text{-}W}>$;
- The presence of residual or seeded impurities further complicates the system behavior.

Unlike the 'toy' model, SOLPS-ITER distinguishes between the different species. Regarding the code outputs, appropriate subscripts are therefore retained in what follows to avoid confusion: $<A_{LCFS}>$ denotes that the quantity 'A' is averaged over the first poloidal ring of computational cells outside the LCFS. In addition, $<T_{e,LCFS}>$ will be used as a proxy for T_{LCFS} (as opposed to $<T_{i,LCFS}>$ which is typically found to be 1.2–1.5 times higher), because the sheath acceleration contributes more to the energy of impinging ions.

Figure 3 provides an example of the variation of $<T_{e,LCFS}>$ and P_{LCFS} through a density scan obtained from SOLPS-ITER simulations for which a detailed description of the setup is given in the following section. Three distinct regimes can be identified. In the medium density range, corresponding to $<n_{e,LCFS}>/n_{GW} \sim 0.2$–$0.8$ (red shaded area in figure 3), the system behavior closely resembles the model described above: $<T_{e,LCFS}>$ remains virtually constant at ~40 eV, while P_{LCFS} scales linearly with $<n_{e,LCFS}>$. However, the system deviates from this behavior both for low and high densities.

At the low-density end, the transition to a new branch (blue shaded area in figure 3) is characterized by a sharp increase in plasma temperature as $<n_{e,LCFS}>$ decreases, so that $<Y_{W\text{-}W}> \gg 1$. The origin of this behavior is as follows: the SOL density decreases to such low values that eroded W begins to escape from the system through the edges of the computational grid (i.e. it travels directly to the wall and adheres there). Therefore, at the limiter surface $<Y_{W\text{-}W}> > 1$ is necessary to maintain the W content within the computational domain, which is achieved by increasing the plasma temperature at the limiter and thus also at the LCFS.

The high-density branch (green shaded are in figure 3) is marked by the rollover of P_{LCFS} with increasing $<n_{e,LCFS}>$. This is due to the frictional coupling between the W and H flows at high density. The high charge states of W are always coupled to H in these simulations through Coulomb collisions due to the high Z, but the associated particle fluxes to the limiter are so low that they do not contribute significantly to the

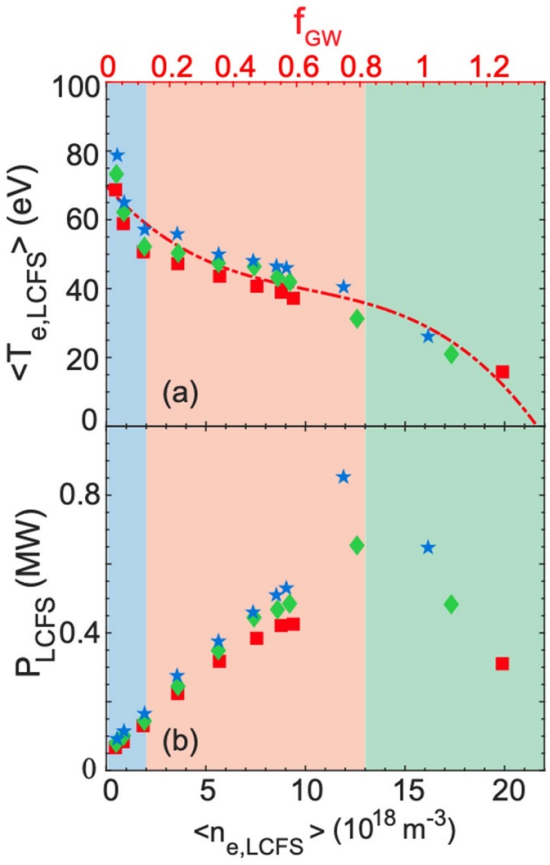

Figure 3. Electron temperature at the LCFS (*a*) and power crossing the LCFS (*b*) as functions of electron density at the LCFS for ITER limiter plasmas with 2.2 (red square markers), 3.3 (green diamond markers), and 4.4 (blue star markers) MW of input power. The data corresponds to 'double λ_q high' transport case introduced in section 4. The ratio of $<n_{\mathrm{e,LCFS}}>$ to n_{GW} is shown at the top of the figure.

erosion. However, as the SOL density increases, lower and lower W charge states couple to the plasma flow. When this process reaches the most common charge states, with $Z \sim (4–6)$, the properties of the system change drastically.

Since $m_{\mathrm{W}} \sim 184\, m_{\mathrm{H}}$, if the H and W fluxes are fully coupled and W remains a trace impurity (i.e. it does not affect the common sound speed and reaches the sheath entrance effectively with the sound speed of H), the W flow becomes supersonic. Under these conditions, impinging W ions can attain the energy required to reach $<Y_{\mathrm{W\text{-}W}}> = 1$ with very little sheath acceleration. This process is further amplified by shallower W impact angles, associated with weakening of the trajectory straightening by the sheath acceleration. As a result, the equilibrium point of $<Y_{\mathrm{W\text{-}W}}> = 1$ shifts to lower plasma temperatures at the limiter and to correspondingly lower $<T_{\mathrm{e,LCFS}}>$. To attain this lower $<T_{\mathrm{e,LCFS}}>$, a higher core dissipation is necessary, driving a transition from an increasing to decreasing trend in $P_{\mathrm{LCFS}}(<n_{\mathrm{e,LCFS}}>)$.

Based on the data from the low and medium density branches (excluding the high-density points) obtained with the SOL transport fitted to the double exponential heat flux profile predicted for ITER inner wall limiter plasmas [13], the following relationship between the equilibrium $<T_{\mathrm{e,LCFS}}>$ and $<n_{\mathrm{e,LCFS}}>$ was found in [1]:

$$< T_{\mathrm{e,LCFS}} > \ (\mathrm{eV}) \ = \ 104.2 \times < n_{\mathrm{e,LCFS}} >^{-0.35} \left(10^{18} \mathrm{m}^{-3}\right). \tag{3}$$

This relationship has been applied in DINA as a boundary condition to force it to converge to the same combinations of $n_{\mathrm{e,LCFS}}$, T_{LCFS} and P_{LCFS} (in the 1D DINA code these quantities are flux surface averaged and $T_{\mathrm{e,LCFS}} = T_{\mathrm{i,LCFS}} = T_{\mathrm{LCFS}}$) as those predicted by SOLPS-ITER. The rationale behind this boundary condition is as follows: a simple equation combining equations (1) and (2) is used to relate P_{LCFS} to the W influx, assuming that $<Y_{\mathrm{W\text{-}W}}>$ is a function of T_{LCFS}. However, instead of introducing T_{LCFS} directly into the $<Y_{\mathrm{W\text{-}W}}>$ calculations (which is equivalent to assuming that the plasma temperature at the erosion zone is the same as at the LCFS and that there is no screening in the SOL, greatly overestimating the W influx), an effective temperature $\alpha(n_{\mathrm{e,LCFS}}) \times T_{\mathrm{LCFS}}$ is used to determine the erosion rate: $<Y_{\mathrm{W\text{-}W}}>(\alpha(n_{\mathrm{e,LCFS}}) \times T_{\mathrm{LCFS}})$. The $\alpha(n_{\mathrm{e,LCFS}})$ is a factor derived from equation (3), accounting for both the shift of the erosion zone with respect to the tangency point (resulting in an offset between T_{LCFS} and the temperature at the region of peak erosion) and neutral W screening in the SOL. The same approach is then used for plasmas with residual impurities, assuming that the profiles of self-sputtering and sputtering by other impurities are alike.

To explore the uncertainties and limitations of this approach, as well as the boundaries of the solution branches described above, a large database of SOLPS-ITER simulations has been constructed. It spans a wide range of transport assumptions, varying the heating power and the number of W charge-states followed, applying some trial prompt redeposition values (validated through detailed simulations with ERO [15]). It also introduces some nitrogen (N) impurity seeding to examine the impact of residual impurities. Simulations with N seeding can be used as a proxy to evaluate the influence of intrinsic O impurity, since the ionization potential and cooling functions of these species are alike. In fact, the deliberate introduction of N has been reported to improve W limiter start-up on WEST [16], although the impurity is introduced rather to assist the current ramp-up phase following X-point formation. It is nevertheless present from the start when the plasma is in limiter configuration.

3. Computational setup

The simulations reported in this paper were conducted using the SOLPS-ITER code package [4], which combines the B2.5 multi-fluid transport code [17] with the EIRENE kinetic Monte-Carlo neutral transport code [18]. The simulations are based on a DINA-generated magnetic equilibrium at $t \sim 4.9$ s of IMAS shot 135011/7, with $I_{\mathrm{p}} = 2$ MA and a toroidal magnetic field $B_{\mathrm{T}} = 5.3$ T. This equilibrium corresponds to a relatively circular limiter plasma just prior to the growth of the limiter plasma before the X-point transition is made. At this

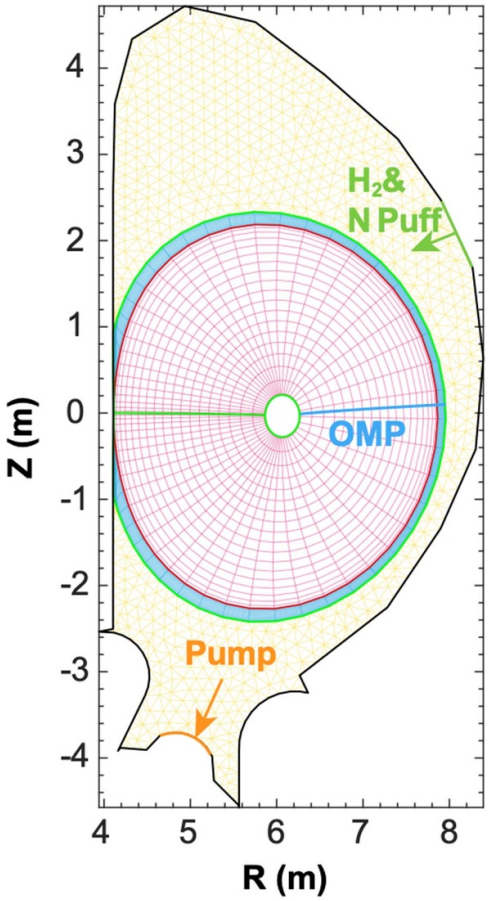

Figure 4. Computational grid for SOLPS-ITER simulations of ITER limiter plasmas: rectangular B2.5 grid (confined region in purple, SOL in blue), triangular outer EIRENE grid (in yellow), H_2 and N injection location (in green), pumping area (in orange). The chord used to plot the OMP profiles is also shown.

point in the DINA start-up scenario, P_{heat} is about 2.2 MW with combined ohmic and EC power.

As shown in figure 4, the computational domain for the SOLPS-ITER simulations comprises a quasi-orthogonal mesh for B2.5 (60 poloidal $\times$ 40 radial cells), which covers the core plasma region and extends several λ_q into the SOL. The EIRENE triangular mesh extends to the FW. The fluid equations are solved on the quasi-orthogonal mesh, while neutral particles can travel throughout the entire vessel. All W charge states up to a given upper limit (see below) are followed as separate fluids, with no charge state bundling. As shown in section 2, in equilibrium, $<c_{\text{W}}>$ in the core self-adjusts to ensure P_{LCFS} such that a SOL plasma is maintained to yield $<Y_{\text{W-W}}> = 1$. Since W radiates very efficiently in the broad region of temperatures from 10 eV to a few keV, it is essential to extend the SOLPS grid deeper into the confined plasma region. If the standard SOLPS approach of extending the grid only a few tens of cm into the core is adopted, either P_{heat} must be adjusted by subtracting the core P_{rad} based on an 'educated guess' or $<c_{\text{W}}>$ would escalate to $\sim 10^{-2}$ in order to provide the required dissipation within the narrow layer of the core included in the simulations. Extending the grid deeper into the core avoids these difficulties and yields meaningful values for $<c_{\text{W}}>$, facilitating direct comparisons with other codes and experiments. Since it is technically impossible with SOLPS-ITER to grid exactly to the magnetic axis, the final $\sim$5 cm ring around it remains unresolved. It is important to note that since $<c_{\text{W}}>$ is typically very low ($\sim 10^{-4}$) and the core volume is large, it becomes crucial to suppress the artificial source of W that originates from the presence of fluid neutrals in SOLPS-ITER, even when the simulation is coupled to EIRENE (see appendix for related technical recommendations).

Unfortunately, building the grids for the vertical limiter case is challenging, especially if both good resolution at the tangency point and wide SOL coverage are required. Since the simulations should also be able to adapt to the narrow λ_q feature ($\sim$4 mm) predicted by the multi-machine scaling [13], resolution near the tangency point is prioritized, resulting in a grid which covers only 10 cm of SOL at the OMP. To ensure that this restriction has no noticeable impact on the solution, a few test simulations with different SOL grid widths were conducted. These scoping simulations used radially constant transport coefficients with $\chi_{\text{e,i}} = 1\ \text{m}^2\ \text{s}^{-1}$ and $D = 0.5\ \text{m}^2\ \text{s}^{-1}$, yielding $\lambda_q \sim 5$ cm which corresponds to the broad, main SOL feature found in the multi-machine scaling [13]. Figure 5 shows that the resulting T_{e} and n_{e} profiles are almost identical for three different SOL extents of $\Delta_{\text{SOL}} = 10$, 20, and 33 cm at the OMP, indicating minimal impact on both core and SOL plasma. In addition, 2D contour plots of total W density confirm that variations in Δ_{SOL} have no noticeable impact on the W distribution throughout the computational domain. A $\Delta_{\text{SOL}} = 10$ cm mesh was therefore selected for further simulations to ensure sufficient resolution at the tangency point while keeping the grid size and its negative impact on the computational time to a minimum. The resulting grid features four computational mesh cells within the first 4 mm of SOL plasma at the OMP and is, therefore, sufficient to resolve the smallest $\lambda_q \approx 4$ mm scale used in our simulations.

The H fuel and seeded impurity (N) are introduced through the main chamber gas puff valve (indicated by the green arrow in figure 4). Plasma density control is achieved by varying the total number of core main plasma ions, following a method similar to that described in [19]. This approach is facilitated by a revised feedback scheme implemented in SOLPS-ITER version 3.0.9 (details provided in the appendix). The feedback-controlled gas puff is balanced by 10% absorption specified around the divertor dome area, with recycling on all other surfaces set to 100% for both H and N. This method, combined with maintaining constant core transport, enables similar solutions for $<n_{\text{e,LCFS}}>$ across different P_{heat} and different SOL transport profiles. This is vital for the computationally rapid construction of a consistent database which spans the desired range of plasma densities.

Unlike H and N, W impurity is introduced into the system via sputtering from the plasma-facing components. It is assumed that the entire FW is covered with W, although the sources from all but the limiter contact areas are negligible and hence the material there only impacts the neutral reflection patterns. The erosion is simulated by EIRENE using the 'Eckstein formulae' [10]. Eroded atoms are either ionized in the plasma or stick to the FW upon contact with 100% probability (thus

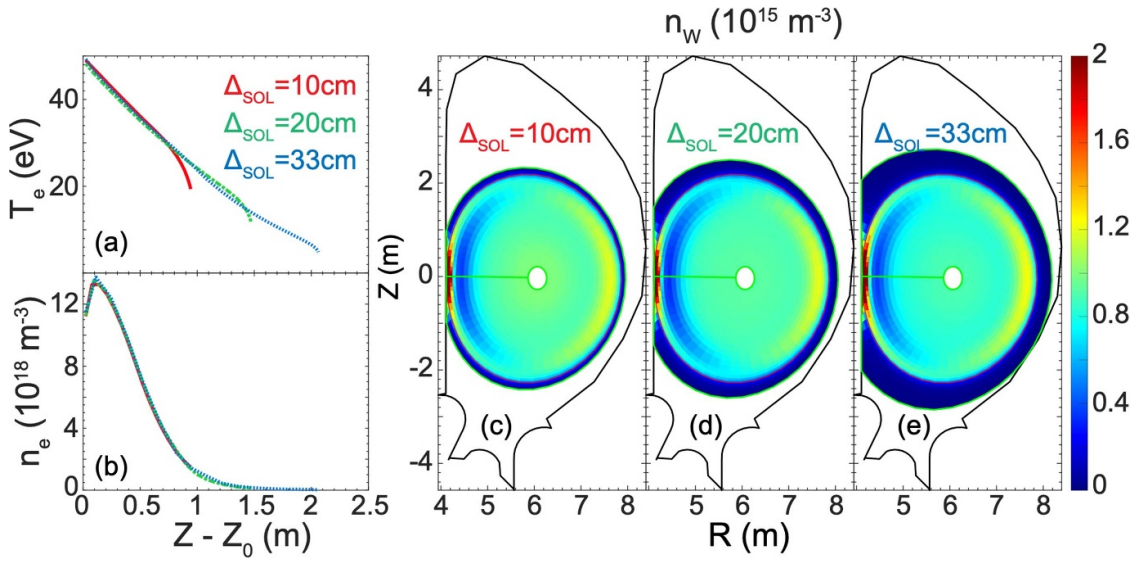

Figure 5. Electron temperature (*a*) and density (*b*) profiles along the limiter surface and 2D distributions of W ion density (*c*)–(*e*) at the same n_{LCFS} obtained in SOLPS-ITER simulations with 3 different grids extending 10, 20, and 33 cm into the SOL (measured at the OMP).

no W reflection). This assumption is justified by the straightening of the W trajectory due to sheath acceleration. As a consequence of the latter, the W^+ distribution over the impinging angle peaks at $\theta \sim 10^\circ$ and extends to $\theta \sim 30^\circ$ [9], whereas the effect is even greater for higher charge states. In this range of θ the reflection probability remains negligible. For instance, at normal incidence, W reflection coefficient $R_{\mathrm{W\text{-}W}}$ initially increases with increasing E_{W}, then reaches its maximum of 0.04 at $E_{\mathrm{W}} \approx 2$ keV and subsequently decreases. Similar trend is observed for the impinging angles $\theta \leqslant 30^\circ$, which are typical for most of the simulated cases, yielding a maximum $R_{\mathrm{W\text{-}W}} \approx 0.1$ and much lower average $R_{\mathrm{W\text{-}W}}$ values [20].

At the targets, the sheath boundary condition is applied based on the Bohm criterion, ensuring that the flow speed at the sheath interface is $\geqslant c_{\mathrm{s}}$, with this criterion applied individually to each fluid (an example of the corresponding input file setup is given in the appendix.). This boundary condition allows for supersonic flow speeds if coupling with other fluids through the drag force is strong enough for this to be achieved. In fact, SOLPS-ITER is most often used with a different boundary condition which imposes a common sound speed for all fluids. This is suitable for low-Z impurities, especially when their concentration is noticeable, and they contribute considerably to the sheath potential formation [21–23]. However, even in such cases, this boundary condition can reduce the impurity flow speed near the sheath, which lacks justification from a physics perspective. In the case of the much higher Z W impurities, this approach leads to very questionable results. Since W remains a trace impurity with a concentration of $\sim 10^{-4}$, the common sound speed is approximately that of the fuel (H in this case). On the other hand, the W/H mass ratio is $\sim$184, resulting in W arriving at the limiter surface with a Mach number of $\sim$14. Therefore, if the common sound speed assumption is adopted, $<Y_{\mathrm{W\text{-}W}}> 1$ is reached even in absence of sheath acceleration, and the high-density branch of the limiter plasma solution described in section II is realized regardless of the input parameters. As a result, the limiter plasma is universally attracted to a detached-like solution with $T_{\mathrm{e}} \sim$ (1–2) eV at the limiter which is clearly not experimentally observed [1, 24, 25].

At the outermost boundary of the B2.5 grid (which does not extend to the FW in these simulations), e-folding decay length boundary conditions are set for temperatures and densities with the same $\lambda_T = \lambda_n = 5$ cm, consistent with the main-SOL λ_q scaling found in [13]. At the innermost boundary (near the magnetic axis) the particle power fluxes for both electrons and ions are set to zero, and particle conservation is imposed for each isonuclear sequence. In practice, this means that the flux of the ion with the highest charge state within a given isonuclear sequence is equal to the flux of the corresponding neutrals reaching the ungridded core region, while zero flux is imposed for the other ions.

The heating power is applied as an electron heating source that combines both EC and ohmic heating and evenly distributed from the center of the grid to the flux surface with normalized radius $\rho = 0.6$ (i.e. the heating power deposited per unit volume in this region remains constant, which cannot be considered a realistic deposition profile in practice). To assess the dependence of the simulation results on P_{heat}, two other values of 3.3 and 4.4 MW in addition to the 2.2 MW DINA reference were also considered. These cases correspond to a higher EC contribution compared to the reference in which ohmic and EC heating are roughly equal. Since, in practice the EC power would be applied close to the magnetic axis to guarantee good absorption and avoid W accumulation (see [1]), the assumed broad heating profile that is already questionable at 2.2 MW becomes even less realistic at higher P_{heat}. However, it has the advantage of a flatter core temperature distribution, which limits the maximum charge state of W ions tracked in the simulations. Since the SOLPS-ITER model is in any case

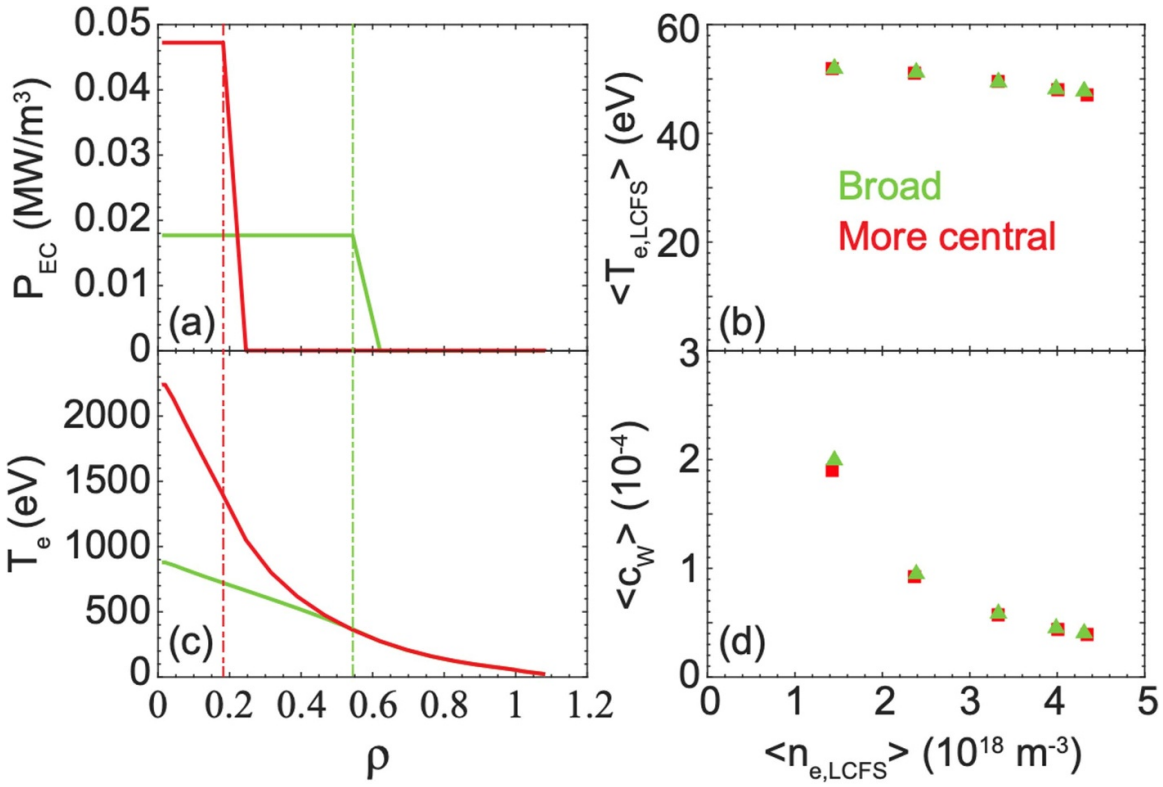

Figure 6. (*a*) The broad (green) and more central EC power (red) deposition profiles used in the SOLPS-ITER simulations to check the impact on the resulting W charge state distributions. (*b*) Electron temperature at the LCFS (*c*) typical OMP electron temperature profiles and (*d*) average W concentration inside the LCFS as functions of $<n_{\mathrm{e,LCFS}}>$ for the two deposition cases (colour coding is preserved).

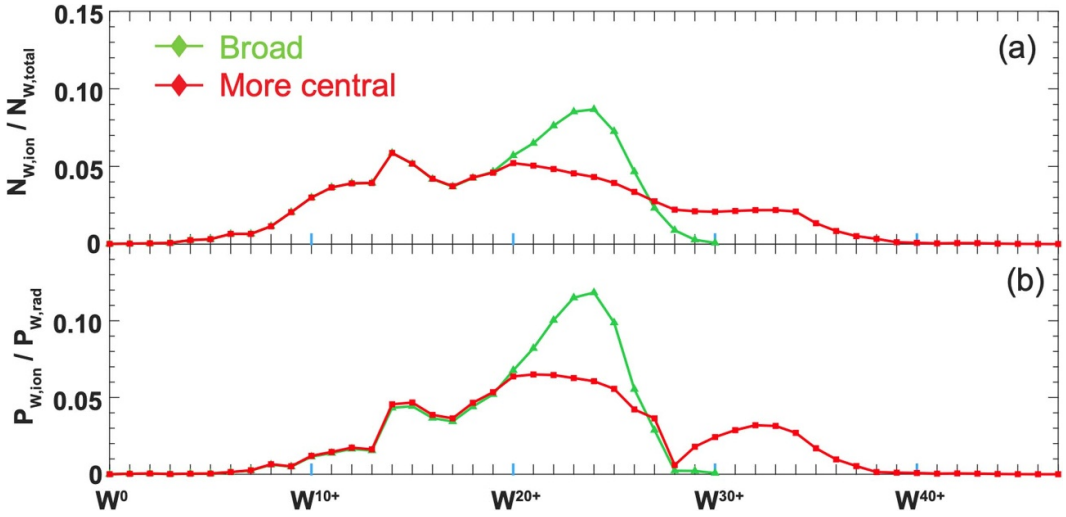

Figure 7. Typical distributions of the W ions over the charge states (*a*) and radiated power fraction from the W charge states (*b*) in the confined region for more central (red) and broad (green) distributions of heating power.

too simple to properly account for the complexities of W transport, it is more a matter of computational ease than capturing correctly the W core density profile. Nevertheless, a specific series of simulations was conducted to check that the broad EC power deposition profile does not strongly impact the SOL plasma solution. Figure 6 compares the results for EC power deposition extending to $\rho = 0.2$ and 0.6, each delivering a total heating power of 2.2 MW.

Based on the core T_{e} achieved in these two scenarios, the highest charge state of W ions followed may be limited to W^{30+} for the broad heating profile and to W^{47+} for the more centrally deposited power. These values were selected according to the ionization energies (1206 eV and 3734 eV for W^{30+} and W^{47+}, respectively). Figure 7 provides an example of the volume averaged W charge state distribution in the confined region and its contribution to the total radiated power in the

two scenarios with identical main plasma density but different heating power distributions. Evidently, the chosen maximum charge states of W are sufficiently high, and as expected, more centrally deposited heating shifts the balance towards a higher average W charge state. Nevertheless, the results shown in figure 6 clearly indicate that the heating profile has negligible impact on the SOL plasma solution and even on $<c_W>$. Based on these findings, the broad heating profile with the maximum W charge state limited to W^{30+} has been used throughout the main simulation database to save computational time.

Finally, drifts were deliberately switched off due to the high computational cost of simulations with 31 ionic species as well as the problems experienced in regions where certain W charge state densities are extremely low. However, the parallel currents necessary to solve the potential equation and obtain a consistent estimate of the sheath potential drop, E_{sh}, were retained. The effects of drifts and associated radial currents are potentially interesting for further development of this work, particularly in cases with a narrow near-SOL parallel heat flux channel, where (as discussed below) the anomalous transport becomes so low that the neglect of classical drift terms cannot really be justified.

4. Transport and heating power variation

The initial ITER limiter case database reported in [1] used the transport assumptions based on fitting a double exponential SOL heat flux profile with $\lambda_q{}^{near} = 4$ mm and $\lambda_q{}^{main} = 50$ mm, chosen so as to be consistent with the parameters used to define the optimum shaping for the original inner FW panel toroidal shaping [13]. In addition, a factor of 2 variation in SOL transport coefficients (the same factor was not applied to the core coefficients) was applied to study sensitivity of the solutions to the transport strength. Unfortunately, this initial database was built using fixed values of the H injection rate, resulting in very different ranges of $<n_{e,LCFS}>$ for the three SOL plasma transport profiles explored. As shown below, this issue, which has now been resolved through the application of a dedicated feedback scheme, obscured the dependence on P_{heat} and led to a very simple $<T_{e,LCFS}>(<n_{e,LCFS}>)$ scaling law. It turns out, in fact, this is a minor drawback since the dependence on P_{heat} is relatively weak and there are greater uncertainties in the simulation setup that have much larger impact (such as the 'prompt redeposition' and residual impurities discussed in later sections).

A second side effect of fitting the double exponential profile and matching it with DINA-like core transport was a steep jump in the transport coefficients at the LCFS. This proved particularly important for the definition of $<n_{e,LCFS}>$ because its value is averaged over the first poloidal ring of computational cells outside of the LCFS. In this area, the density evolved sharply making the resulting $<n_{e,LCFS}>$ overly sensitive to the local grid resolution and cross-field transport variation.

There is, however, a more serious concern with using the double exponential profile derived in [13]. The multi-machine database which was constituted to derive the scaling for ITER consisted of fully formed stationary limiter cases with values of I_p relatively close to the nominal value for each machine with typical safety factors in the range $q_{95} \sim 3$–6. In the ITER case when B_T is at its nominal value (5.3 T), the maximum current in the limiter ramp-up limiter phase will be $I_p \sim 3$ MA, a factor of 5 lower than the maximum value characteristic of burning plasma diverted discharges (15 MA). At the DINA scenario time-slice chosen for the SOLPS-ITER simulations, $q_{95} \sim 11$, resulting in a very large connection length, $L_c \sim 200$ m on the first SOL flux surfaces, whereas the plasmas used for the scaling derivation had L_c values of at most a few tens of meters. To reproduce the desired $\lambda_q{}^{near} = 4$ mm thus requires a radial heat transport coefficient of $\chi_{e,i} \sim 0.01$ m^2 s^{-1} (assuming $D = 0.5\chi_{e,i}$). Under such conditions, simulations without classical drift terms included become questionable since anomalous transport is no longer dominant.

To address this issue, a significantly wider range of SOL transport parameters was explored compared to the initial study in [1]. The new simulations include two sets of SOL transport profiles, both combined with the same flat core transport profile, where the heat and particle diffusion coefficients are $\chi_{e,i} = 1$ m^2 s^{-1} and $D = 0.5$ available at:, respectively. The first set (referred to as 'single λ_q' in what follows) does not try to replicate the double exponential scaling at all. Instead, it uses the transport coefficients similar to the baseline ITER divertor H-mode transport assumptions, prolonging the radially constant values $\chi_{e,i} = 1$ m^2 s^{-1} and $D = 0.5$ m^2 s^{-1} from the confined region into the SOL (labelled as 'mid' in the following figures containing results from the database). In addition, a factor of 2 variation (i.e. $\chi_{e,i} = 2$–0.5 m^2 s^{-1} and $D = 1.0$–0.25 m^2 s^{-1}) is applied in the SOL, adding 2 more transport profiles to the 'single λ_q' set (labeled as 'high' and 'low' in the following database figures).

The second set, referred to as 'double λ_q', includes a narrow barrier-like decrease in transport extending 1–2 cm into the OMP SOL from the LCFS, similar to the old double exponential cases (presented in [1]), but with a less pronounced drop. The width of the barrier is varied to obtain 2 different values of $\lambda_q{}^{near}$, gradually approaching the 4 mm value derived from the multi-machine scaling. Similarly to the 'single λ_q' set, D is fixed to $\chi_{e,i}/2$ for all the 'double λ_q' profiles. Finally, we nevertheless retain the old database points corresponding to fitting as closely as possible the double exponential profile with $\lambda_q{}^{near} = 4$ mm and $\lambda_q{}^{main} = 50$ mm, but noting the caveat that this set has a different core transport (both D and χ increasing parabolically from the magnetic axis to the LCFS) and, in addition, sets $D = \chi$ in SOL. The ensemble of transport profiles and corresponding effective λ_q values is shown in figure 8, demonstrating that the new, significantly expanded database covers a wide range of λ_q from 4 to 50 mm (thus covering the full span of $\lambda_q{}^{near}$ and $\lambda_q{}^{main}$ found in [11]). For each of the three sets of transport choices simulations have been performed at the three values of $P_{heat} = 2.2$, 3.3, and 4.4 MW.

Figure 9 illustrates the dependence on density (equivalent to H fueling rate) throughout the database of three key parameters: $<T_{e,LCFS}>$, $f_{rad} = P_{rad}/P_{heat}$, and $<c_W>$. For

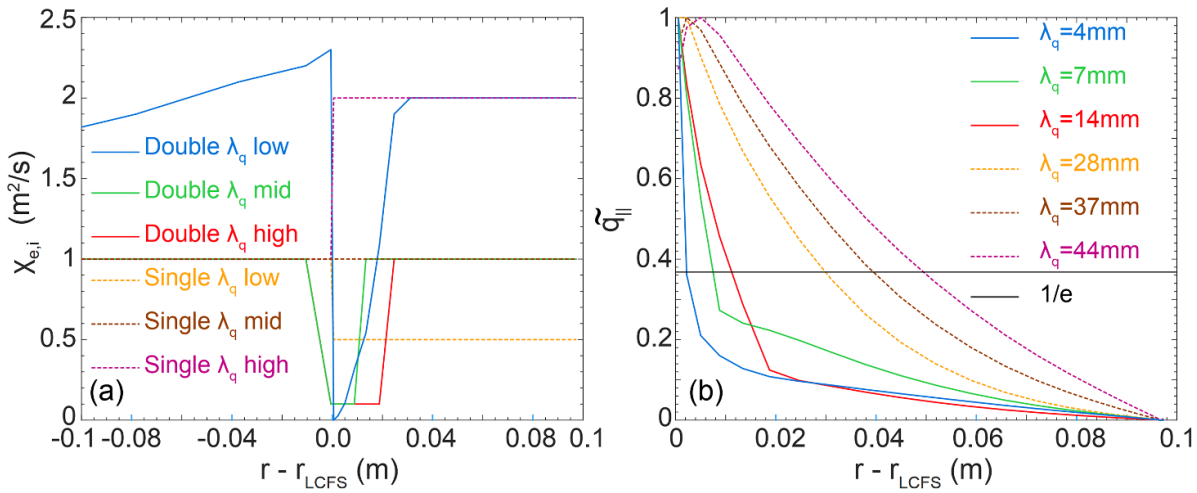

Figure 8. Heat diffusion profiles (*a*) used in the study with particle diffusion is set to half the heat diffusion for all cases except the lowest transport case (shown in blue) where they are equal. The normalized total heat flux profile at the OMP and associated values of λ_q are shown in (*b*).

convenience, the cases with 'single λ_q' and 'double λ_q' transport profiles are shown in different frames, with the range where 'single λ_q' overlaps the wider 'double λ_q' parameter space. Although λ_q varies by an order of magnitude across the database, the results are relatively insensitive to this parameter. In practice, the region of most interest lies within the range $<n_{\mathrm{e,LCFS}}>/n_{\mathrm{GW}} = 0.15$–$0.5$, since it will be hard to couple significant EC power to densities much lower than a few 10^{18} m^{-3} (see e.g. [26, 27]), while the high-density end will be limited by the approach to the Greenwald limit [28]. It is clearly seen in figure 9 that for all the transport assumptions, this range corresponds to the medium density branch described in detail in section 2. Typical values of $<c_{\mathrm{W}}>$ and f_{rad} are (1–2) $\times$ 10^{-4} and (0.7–0.8), respectively.

It is also of note that, as predicted for the medium density branch, the dependence of $<T_{\mathrm{e,LCFS}}>$ on $<n_{\mathrm{e,LCFS}}>$ is rather flat, and there is a clear correlation between $<T_{\mathrm{e,LCFS}}>$ and P_{heat} that was neglected equation (3). Taking this now into account, the least square regression performed for the 'double λ_q' series, excluding the points with $<n_{\mathrm{e,LCFS}}> > 0.5n_{\mathrm{GW}}$ gives:

$$\lambda_q = 4\ \mathrm{mm}:$$
$$<T_{\mathrm{e,LCFS}}>(\mathrm{eV}) = (69.4 \pm 7.9) \times <n_{\mathrm{e,LCFS}}>^{-0.26\pm0.03} \left(10^{18}\mathrm{m}^{-3}\right) \times P_{\mathrm{heat}}{}^{0.23\pm0.08}\,(\mathrm{MW}),\ R^2 = 0.89 \quad (4)$$

$$\lambda_q = 7\ \mathrm{mm}:$$
$$<T_{\mathrm{e,LCFS}}>(\mathrm{eV}) = (54.5 \pm 3.0) \times <n_{\mathrm{e,LCFS}}>^{-0.15\pm0.01} \left(10^{18}\mathrm{m}^{-3}\right) \times P_{\mathrm{heat}}{}^{0.19\pm0.05}\,(\mathrm{MW}),\ R^2 = 0.98 \quad (5)$$

$$\lambda_q = 14\ \mathrm{mm}:$$
$$<T_{\mathrm{e,LCFS}}>(\mathrm{eV}) = (49.7 \pm 4.2) \times <n_{\mathrm{e,LCFS}}>^{-0.18\pm0.02} \left(10^{18}\mathrm{m}^{-3}\right) \times P_{\mathrm{heat}}{}^{0.20\pm0.07}\,(\mathrm{MW}),\ R^2 = 0.96. \quad (6)$$

The resulting $<T_{\mathrm{e,LCFS}}>(<n_{\mathrm{e,LCFS}}>)$ dependencies at fixed $P_{\mathrm{heat}} = 3.3$ MW are shown in figure 9. It can be seen that although with increasing λ_q, $<T_{\mathrm{e,LCFS}}>$ decreases due to the decreasing T_{e} offset between the LCFS and peak erosion area, the functional dependence on both $<n_{\mathrm{e,LCFS}}>$ and P_{heat} does not change much. The $\lambda_q = 4$ mm case exhibits somewhat steeper dependence on $<n_{\mathrm{e,LCFS}}>$ because of a very sharp drop in transport coefficients near the LCFS (see figure 8) discussed in the beginning of this section.

5. Impact of 'prompt redeposition'

In the SOLPS-ITER simulations the erosion is calculated using EIRENE. The impinging W ion is sampled from a drifting Maxwellian distribution and is then accelerated by the sheath potential E_{sh} towards the surface. The sheath potential is calculated self-consistently inside the B2.5 plasma solver, and for the simulations reported in this paper, the typical value of E_{sh} is in the range of (2–2.5) T_{e}. Neither gyration nor surface roughness are accounted for in this model. The average charge of impinging W ions in the new database is $<Z_{\mathrm{W}}> \geqslant 6$, except for the high density cases which are of little practical interest due to the high $<n_{\mathrm{e,LCFS}}>$ (typically $\gg 0.5 \times n_{\mathrm{GW}}$). This results in almost normal incidence of W ions and an underestimation of $<Y_{\mathrm{W\text{-}W}}>$. However, it was shown in [9] that for heavy W ions the straightening of the impinging ion trajectories by sheath acceleration remains dominant even when surface roughness and ion gyration are considered. Almost normal incidence of W in EIRENE simulations should therefore be reasonable.

Nevertheless, EIRENE is missing a key component: prompt redeposition of W, a process by which eroded W atoms are ionized in the immediate vicinity of the surface and return to it under the influence of gyro-motion and the sheath electric field [14]. In principle, these promptly redeposited W particles

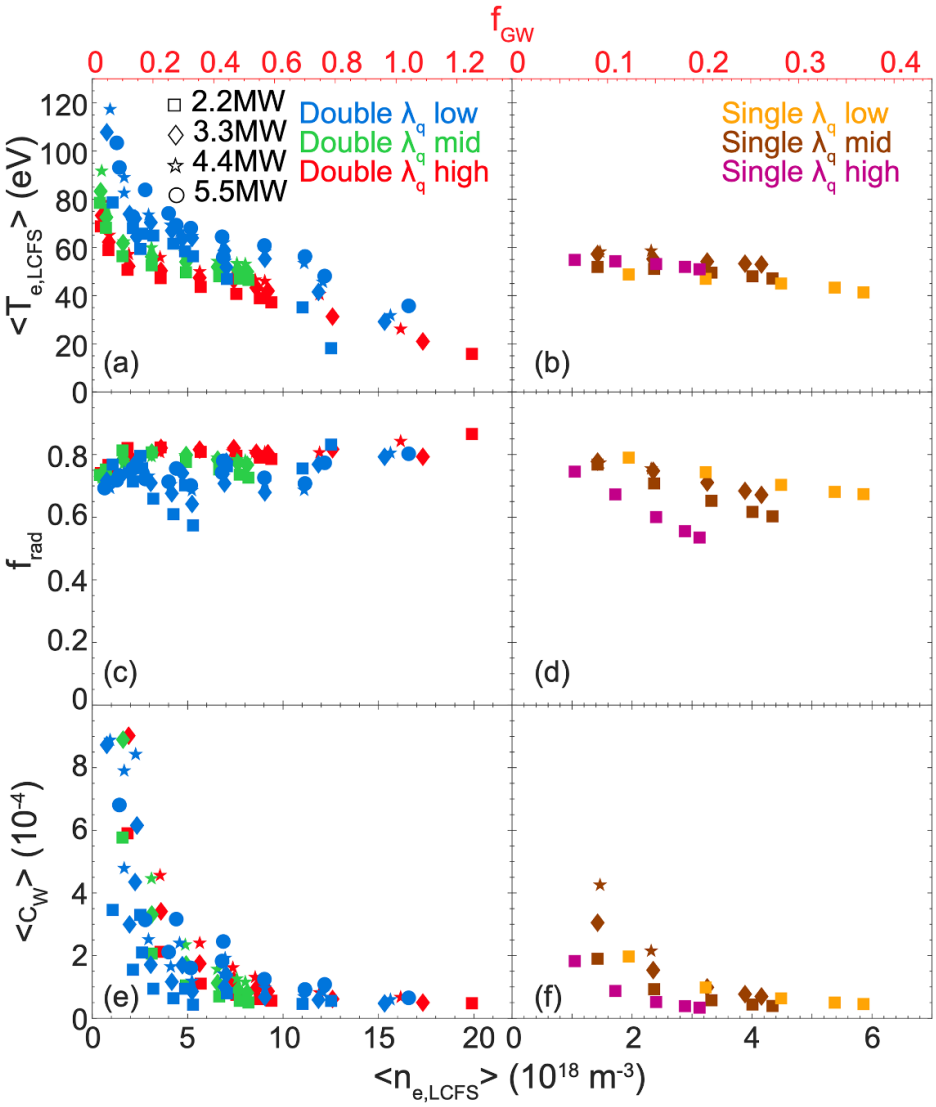

Figure 9. Electron temperature at the LCFS (*a*), (*b*), the fraction of heating power radiated (*c*), (*d*) and average W concentration (*e*), (*f*) inside the LCFS as functions of electron density at the LCFS obtained in simulations with different transport profiles (shown in figure 8, with the same color scheme). The cases with 'double exponential' transport profiles are shown on the left (where the double λ_q high series is the same as the data presented in figure 3(*a*)), and with the 'single exponential' transport profiles on the right. For reference, the upper abscissa provides LCFS density values normalized to the Greenwald density [28] $f_{\mathrm{GW}} = <n_{\mathrm{e,LCFS}}>/n_{\mathrm{GW}}$.

should not enter the fluid equations in the B2.5 part of SOLPS-ITER, because for these particles the ionization and redeposition occurs on the spatial scale that is not resolved by the fluid code. The standard way of treating it in the SOLPS suite of codes is by application of a multiplicator to the corresponding erosion source [29, 30].

There are several analytical models with which the fraction of promptly redeposited eroded atoms can be estimated (see e.g. [14, 31]). However, these models neglect the electric field and do not allow for arbitrary magnetic field orientation. As a consequence, a more accurate evaluation of the prompt redeposition fraction is typically performed using Monte-Carlo kinetic simulations [32, 33]. Here, it has been estimated at the limiter surface using the 3D Monte-Carlo plasma–wall interaction and impurity transport code ERO [15].

The ERO modelling was restricted to a localized simulation volume at the ITER inner wall, which functions as a limiter during the current ramp-up phase, covering a vertical region between $z = -0.5$ m to $z = +0.5$ m (see figure 10), a radial width of 0.1 m and a toroidal length of 1 m. Two plasma backgrounds with medium and high $<n_{\mathrm{e,LCFS}}>$ from the initial SOLPS-ITER simulation database first introduced in [1] with 'double λ_q' fitted to the multi-machine scaling [13] have been studied. In figure 11 the profiles of T_{e} and n_{e} along the inner wall (from $z = -1$ m to $z = 1$ m) are shown for both cases. It shows that the region used for the ERO simulations covers the most important area, where the densities and temperatures are at their highest values, whereas outside the simulated region, profiles do not change much. The medium and high density backgrounds have maximum values of T_{e} and n_{e} of (65 eV,

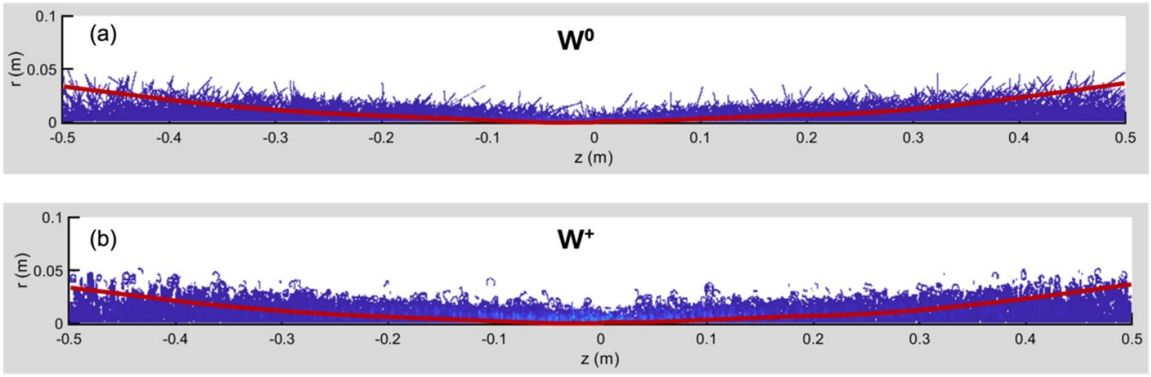

Figure 10. 2D distribution of (*a*) tungsten atoms and (*b*) singly charged tungsten ions in front of the inner wall (acting as a limiter) for the medium plasma density. The red curve indicates the LCFS.

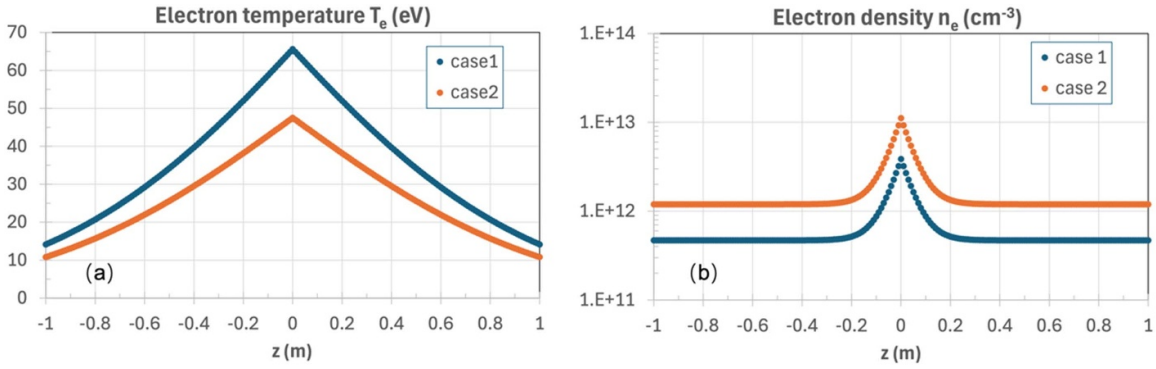

Figure 11. Profiles of (*a*) electron temperature and (*b*) electron density along the inner wall for two cases with medium (case 1) and high (case 2) limiter plasma densities.

4×10^{18} m^{-3}) and ($T_e \sim 47$ eV, $n_e \sim 1 \times 10^{19}$ m^{-3}) respectively. The FW shaping was not considered in these simulations (although ERO is capable of treating complex wall structures), with a flat surface being assumed for simplification.

It is well known that the sheath electric field is an important parameter influencing the prompt redeposition of W. In ERO, the electric potential Φ within the sheath is described by the following formula [34]:

$$\Phi = \Phi_0 \times f_d(\alpha_B) \times \mathrm{e}^{-d/2\times\lambda_D} + \Phi_0 \times (1 - f_d(\alpha_B)) \times \mathrm{e}^{-d/r_L} \quad (7)$$

with $\Phi_0 \sim 3 \times T_e$ and where λ_D is the Debye length, r_L the gyration radius of plasma ions, d the normal distance from the surface and f_d a parameter which depends on the magnetic field angle α_B ($f_d = 1$ for a magnetic field perpendicular to the surface. For shallower magnetic field attack angles, $f_d \to 0$ and the potential mainly scales with r_L, which applies to the cases under consideration here with very shallow magnetic field line angles ($\sim$0.1°) at the inner wall). The electron density and temperature are assumed to be constant within the sheath; the possible influence of non-uniform sheath plasma parameters has been discussed e.g. in [35].

Sputtered W atoms start at the surface with a Thompson energy and a cosine angular distribution. An anomalous cross-field diffusion coefficient (D_W) of 1 m^2 s^{-1} is assumed for the traced W, the ionization of which is calculated using rate coefficients from ADAS [36]. Particles returning to the surface are reflected according to reflection coefficients from SDTrimSP [37]. Non-reflected particles are deposited on the surface. If the migration time of the particle until redeposition is shorter than its gyration time, the corresponding particle is considered promptly redeposited. Since the focus is solely on estimating the fraction of promptly redeposited particles, the details of W gross erosion along the surface are not discussed here.

Figure 10 shows the distribution of W atoms and singly charged W ions above the inner wall surface, integrated along the toroidal direction, for the medium density case. Since the density and temperature peak near the tangency point ($z = 0$), penetration of W is lowest in that region. The fraction of promptly redeposited W particles (f_{redep}) along the surface is illustrated in figure 12 for the two chosen plasma backgrounds. Near $z = 0$, f_{redep} is $\sim$60% for the medium and $\sim$80% for the high density case. Further away from the tangency point, f_{redep} decreases to $\sim$20% and $\sim$40% respectively for the two cases. The surface-averaged f_{redep} is 27% for the medium and 43% for the high density case. The larger f_{redep} in the high density case is the result of the dominance of the increase in n_e (leading to higher ionization and thus shorter penetration

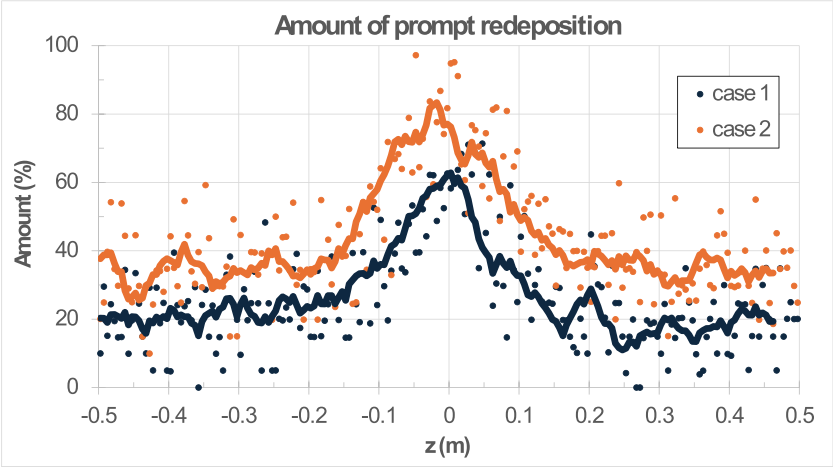

Figure 12. The fraction of local tungsten erosion 'promptly redeposited' along the inner wall for two cases of the medium (case 1) and high (case 2) limiter plasma density. The solid lines are the result from moving average over 8 points.

depth of W) over the decrease in T_e (leading to lower ionization and thus larger penetration depth). It is important to note that the modelling also provides the overall amount of local redeposition (prompt and non-prompt) resulting in surface-averaged values of 80% for the medium and 89% for the high density case.

Because the anomalous cross-field diffusion coefficient for W in the ERO simulations does not match the one used in SOLPS-ITER simulations, another test run with D_W set to 0 $m^2\ s^{-1}$ was performed. Virtually no difference was found for the 'prompt redeposition'. This is unsurprising given that the process takes place on the timescale of one gyration (by definition) and major factors here are the magnetic and electric fields as well as the angular and energy distributions of the sputtered atoms, not radial diffusion. This proves that the estimates of prompt redeposition are robust enough with respect to the anomalous diffusion coefficient and can be extrapolated to all the SOLPS simulations in this paper, which imposed D_W ($=D$) in the range of 0.05–1 $m^2\ s^{-1}$.

To assess the influence of prompt redeposition on the limiter plasma equilibrium, a series of dedicated simulations with W sputtering yield reduced by 35% (a value in-between the two cases studied above) uniformly all over the limiter surface were conducted. For this test, two different transport profiles were used: (i) flat 'single λ_q' transport profile (shown in brown in figure 8) and (ii) widest 'double λ_q' transport profile (shown in red in figure 8). We note that due to the more peaked n_e and T_e profiles, the 'double λ_q' transport case naturally exhibits high variation in prompt redeposition along the surface. It is therefore less well-suited to the application of a simple uniform redeposition assumption.

Figure 13 compares the cases with reduced erosion mimicking the prompt redeposition and the corresponding transport cases from the database described in section 4. Unsurprisingly, the change in effective sputtering yield, which determines the equilibrium point of the system, has a greater impact on the solution than an order of magnitude change in λ_q. With reduced erosion rate, the equilibrium condition $<Y_{W\text{-}W}> = 1$ requires higher plasma temperature in the vicinity of the limiter surface, which results in a ∼30% increase in $<T_{e,LCFS}>$ from (40–60) eV without prompt redeposition to (70–90) eV. This naturally requires higher P_{LCFS}, hence a decrease in f_{rad}. With prompt redeposition f_{rad} can fall below 0.5, whereas without it, $f_{rad} > 0.6$ and remains in the range (0.7–0.8) for majority of the cases. The average charge state of W impinging on the limiter rises by ∼30%, although the ratio between $<Z_W>$ at the LCFS and at the limiter remains virtually unchanged at ∼1.5.

A closer look at the erosion profiles for a few cases with and without prompt redeposition at similar $<n_{e,LCFS}>$ (marked with blue squares in figure 13) is given in figure 14. As expected, the erosion profiles are peaked further away from the tangency point (where the plasma temperature is highest) resembling the particle flux profiles. For the 'double λ_q' transport profiles, the erosion peak is closer to the tangency point as the transport in the near SOL is significantly reduced compared to the 'single λ_q' transport profile. Prompt redeposition does not much affect the erosion profile, but it does decrease the total erosion since less W is needed to provide the P_{rad} required to achieve the equilibrium P_{LCFS}.

A further observation from figure 14 is that, with prompt redeposition, the erosion is no longer limited to W self-sputtering since the plasma temperature at the limiter is high enough for H ions accelerated through the sheath to exceed the sputtering threshold ∼402 eV. For the assumed prompt redeposition of 35%, the W self-sputtering still dominates with ∼4%–7% of W being sputtered by H, which given the ratio of impinging H and W ion fluxes implies $<Y_{H\text{-}W}> \approx 5 \times 10^{-5}$, which under given conditions originates from the tail of the Maxwellian distribution.

It should be noted that these simulations are only meant to illustrate the magnitude of the effect that prompt redeposition will have on the plasma solution and put it into perspective against the other uncertainties (such as SOL transport and impurity content). The introduction of the flat (target averaged) prompt redeposition modifier on Y_W in all the cases

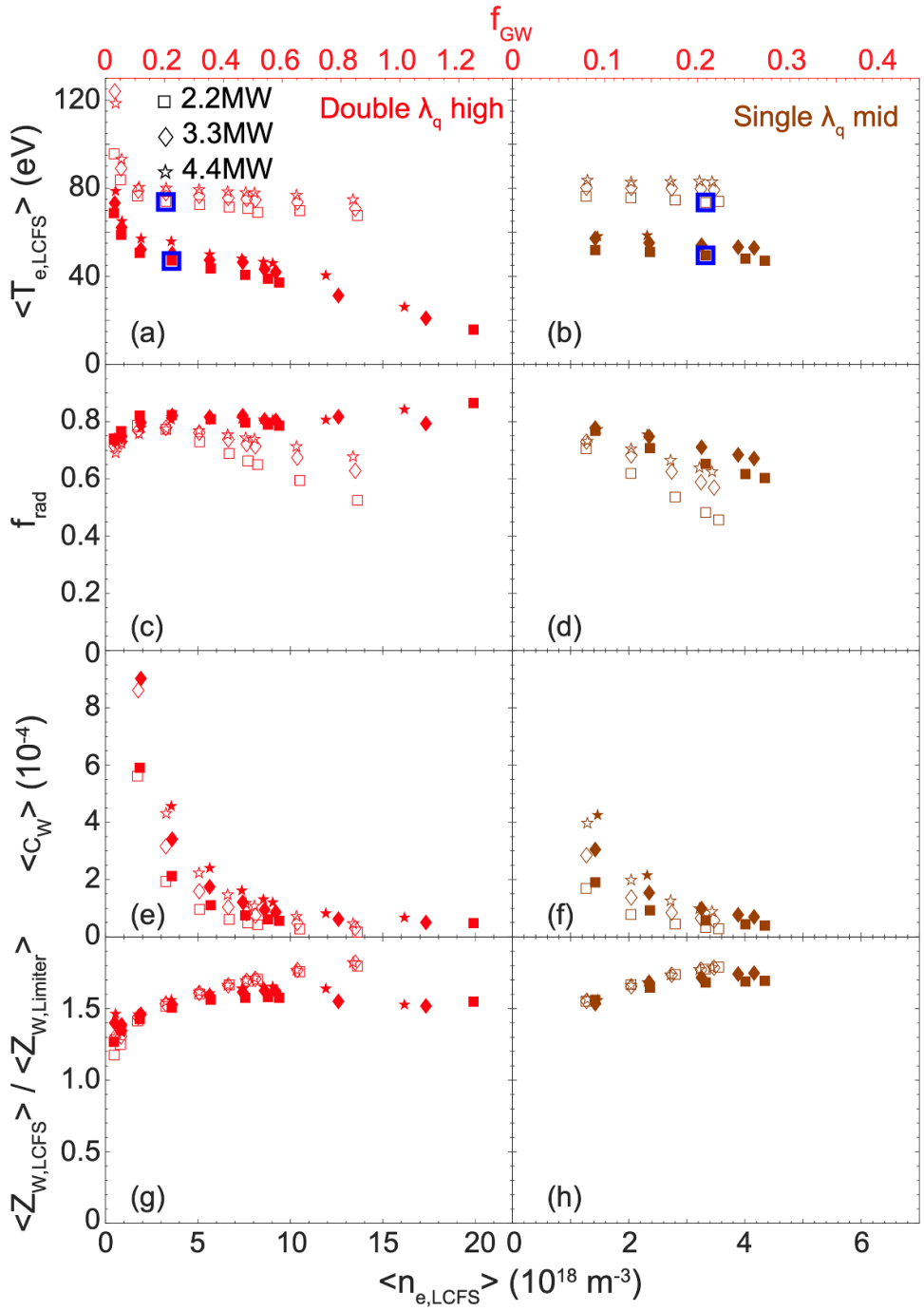

Figure 13. (*a*), (*b*) Electron temperature at the LCFS, (*c*), (*d*) fraction of heating power radiated, and (*e*), (*f*) average W concentration inside the confined region and ratio of average W ion charge at the LCFS to the average charge of W ions impinging the limiter (*g*) and (*h*) as functions of $<n_{e,LCFS}>$ obtained in simulations with different transport profiles (shown in figure 8, with the same color scheme) with (empty symbols) and without (full symbols) 'prompt redeposition'. The cases with 'double exponential' transport profiles are shown on the left and with the 'single exponential' transport profiles on the right. The blue squares specify the cases selected for detailed analysis. For reference, the upper abscissa provides LCFS density values normalized to the Greenwald density [28] $f_{GW} = <n_{e,LCFS}>/n_{GW}$.

misses both the spatial resolution of prompt redeposition and its increase with increasing $<n_{e,LCFS}>$. Moreover, the modifier on Y_W changes the background plasma solution that was used to obtain the modifier itself. To properly model the prompt redeposition effect, a simple model such as those proposed in [14, 31] should at least be embedded into the simulations allowing for the self-consistent and spatially resolved treatment (even if it will not be as complete and sophisticated as in the ERO code). Such an option is available in SOLPS-ITER package on B2.5 side [38], but it is only applicable to simulations with fluid neutrals and further development is required to incorporate it into the EIRENE.

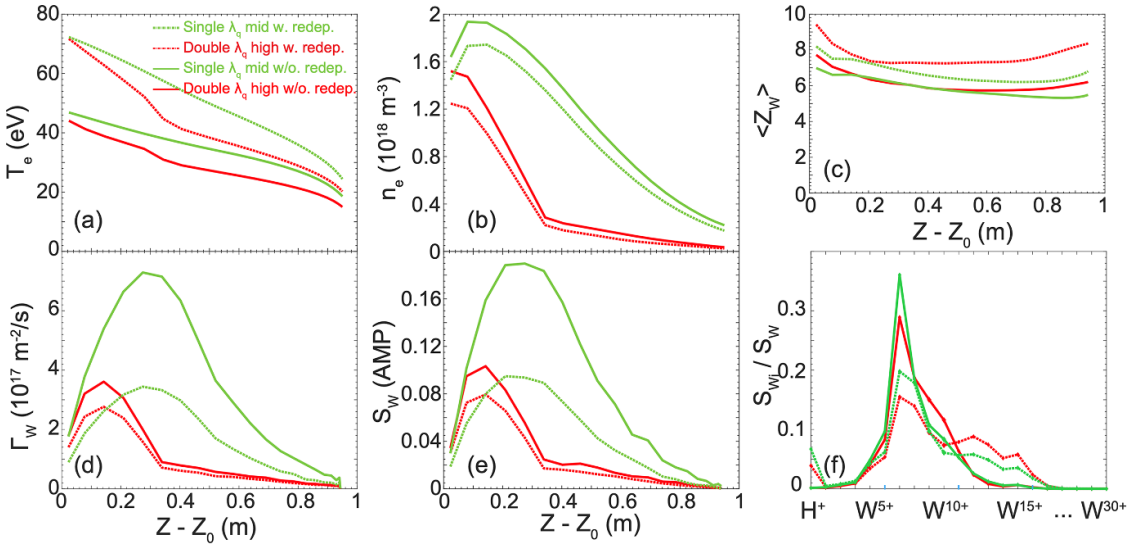

Figure 14. Electron temperature (*a*) and density (*b*), average charge of impinging W ions (*c*), W ion flux (*d*), W erosion source (*e*) profiles along the limiter surface and contribution of different ions to the total erosion source (*f*) for 4 different cases marked in figure 13. In red—'double exponential' transport profiles with (solid line) and without (dashed line) 'prompt redeposition' (marked in figure 13(*a*)); in green—'single exponential' transport profiles with (solid line) and without (dashed line) 'prompt redeposition' (marked in figure 13(*b*)).

Nevertheless, the flat 35% modifier to Y_{W} used here is a reasonable upper bound estimate for the effect since the several orders of magnitude difference in the impinging H and W fluxes leave little room for a further rise of $<T_{\mathrm{e,LCFS}}>$ with increasing prompt redeposition fraction before the sputtering by H becomes dominant and the system becomes attracted to $<Y_{\mathrm{W\text{-}W}}> + <Y_{\mathrm{H\text{-}W}}> \times \Gamma_{\mathrm{H}}/\Gamma_{\mathrm{W}} = 1$, where $\Gamma_{\mathrm{H}}/\Gamma_{\mathrm{W}}$ is the ratio of impinging H and W ion fluxes. We also note that in deuterium (D) plasma this transition will happen at lower $<T_{\mathrm{e,LCFS}}>$ since W sputtering by D is roughly twice as efficient (and starts at a lower threshold $\sim$ 204 eV). Less impact on f_{rad} is thus expected in D plasmas.

6. Impact of residual impurities and/or impurity seeding

Up to this point, only pure H plasma in contact with W limiter has been considered. However, following breakdown, the plasma inevitably contains some residual amount of oxygen and other low-Z impurities. In the worst-case scenario, the radiative barrier formed by these impurities prevents plasma burnthrough, hindering the transition to the current ramp-up phase [26]. This problem is significantly exacerbated when exchanging the FW material from Be since Be is an excellent O getter, reducing the residual O concentration during the plasma initiation phase [1]. To mitigate this problem, a new boronization system is being developed and will be installed on ITER as part of the re-baseline [39]. A further possible source of impurity may originate from intentional seeding; N gas puffing was found useful on WEST to facilitate plasma current ramp-up with a W FW by increasing core plasma temperature, improving MHD stability and achieving lower core $<c_{\mathrm{W}}>$ right after the transition to the divertor phase [16, 24].

Setting up a SOLPS-ITER simulation with realistic O sources and sinks in the ITER limiter phase is virtually impossible, because of the uncertainties in the source and sink description. Oxygen is present both in residual gas before the breakthrough and released from the plasma facing components. Additionally, it is also absorbed by the boron layer, which evolves from shot to shot. On the other hand, the content of seeded impurities such as N can be reliably controlled through the feedback on the seeding rate, despite the uncertainties associated with the surface chemistry. We therefore focus on N seeded cases which can nevertheless be viewed as a proxy to the limiter plasma scenarios with similar O concentration (because the charge of the nuclei, the first ionization potential and cooling functions of N and O are very similar).

Since these code runs must now include H, W and N species, they are computationally more demanding and less numerically stable than those of the rest of the database and so the simulations are limited to a single $P_{\mathrm{heat}} = 2.2$ MW and only for a flat 'single λ_q' transport profile with $\chi_{\mathrm{e,i}} = 1$ m^2 s^{-1} and $D = 0.5$ m^2 s^{-1}. The total number of N ions in the core, N_{N} was fixed to 0.1% or 0.5% of the total number of H ions in the core (N_{H}) at the lowest density simulated $<n_{\mathrm{e,LCFS}}>/n_{\mathrm{GW}} \sim 0.15$. This corresponds to average core N densities of $<n_{\mathrm{N}}> \sim 6.75 \times 10^{16}$ and 3.3×10^{17} m^{-3} respectively, referred to as low and high N seeding cases in what follows. Density scans are then performed by gradually increasing N_{H}, with N_{N} maintained at the fixed levels defined above by means of the feedback scheme regulating the N seeding rate. For both values of N_{N} two density scans were performed with and without prompt redeposition (mimicked according to the approach described in section 5).

In figure 15 the results of N seeded simulations are shown along with similar unseeded cases. The N contribution to W erosion changes the attractor of the system from $<Y_{\mathrm{W\text{-}W}}> = 1$

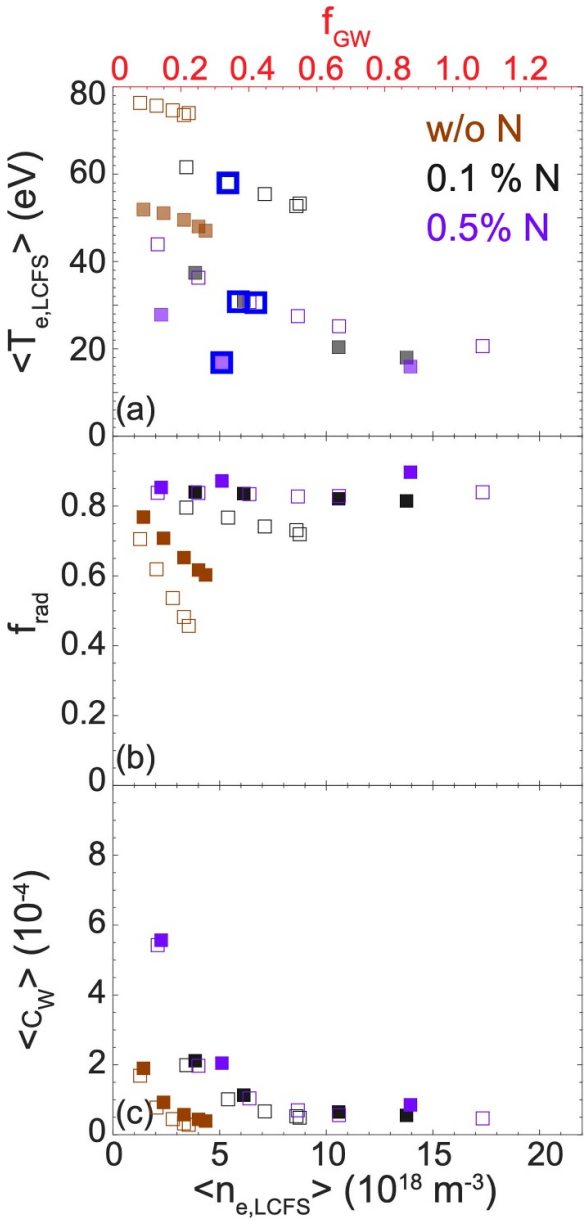

Figure 15. Electron temperature at the LCFS (*a*), the fraction of heating power radiated (*b*) and average W concentration (*c*) inside the confined region as functions of $<n_{e,LCFS}>$ obtained in simulations with different flat 'single exponential' transport profile (shown in figure 8 in brown) without N and N content fixed to 0.1 and 0.5% of total H content at $<n_{e,LCFS}>/n_{GW} \sim 0.15$. Cases without (full symbols) and with (empty symbols) 'prompt redeposition' are considered. In all cases $P_{heat} = 2.2$ MW. The blue squares specify the cases selected for detailed analysis. For reference, the upper abscissa provides LCFS density values normalized to the Greenwald density [28] $f_{GW} = <n_{e,LCFS}>/n_{GW}$.

to $<Y_{W\text{-}W}> + <Y_{N\text{–}W}> \times \Gamma_N/\Gamma_W = 1$, where Γ_N/Γ_W is the ratio of impinging N and W ion fluxes, reducing the equilibrium $<T_{e,LCFS}>$. It can be seen that even a modest quantity of N is enough to offset the increase in the equilibrium $<T_{e,LCFS}>$ provided by the prompt redeposition. With increasing N_N and/or N_H, the equilibrium $<T_{e,LCFS}>$ drops further and saturates at ~20 eV. Moreover, even with low seeding, f_{rad} increases to ~0.8, saturating at this level. For the series with high N seeding and prompt redeposition included, figure 16 shows the total radiated power in the confined region, along with contributions from W and N separately. As $<n_{e,LCFS}>$ increases, a greater fraction of W radiation is replaced with N radiation, but the total radiation remains virtually the same. Therefore, with higher $<n_{e,LCFS}>$ the radiation losses shift from the deep core, where W radiation is most efficient to the edge where N radiates. This interplay between radiation of W and O/N can, under certain conditions intensify the edge plasma cooling, which can eventually trigger MHD instabilities. The presence of residual or seeded impurities can thus make the system more susceptible to radiative collapse.

Figure 17 compares the erosion profiles for 4 cases with low and high N seeding, with and without prompt redeposition at $<n_{e,LCFS}> \sim 5 \times 10^{18}$ m^{-3}. In all 4 cases the flux profiles of W and N ions to the limiter surface have a similar shape and the resulting erosion profiles are also alike. This justifies the approach described in section 2 used to modify the DINA boundary conditions to account for W limiter start-up in the scenario design [1, 6] (namely to presume a similar correction to Y_W for all the species leaving the confined region). The contribution from W self-sputtering dominates in all the cases. The highest contribution from impurity was found in the case with high N content and no prompt redeposition where N is responsible for roughly 30% of the total W erosion. The balance shifts further in favor of W self-sputtering if prompt redeposition is accounted for. As it was shown in previous section with prompt redeposition considered T_e at the erosion region increases. Since sheath acceleration is $\sim Z_i \times T_e$ increasing T_e amplifies the W self-sputtering more than N–W sputtering due higher average charge of W ions involved in the sputtering process (see figure 17).

7. Summary

Due to the very high radiative fractions which can be associated with core plasma W impurity concentrations the transition from Be to W as ITER FW material in the new 2024 re-baseline introduces a new potential risk to successful plasma start-up in the limiter phase of the current ramp. To assess this issue, time-dependent simulations of this early ramp-up phase, accounting for the plasma shape and current evolution, main plasma and impurity transport, coupled to an accurate SOL plasma solution, are required. Since core and edge timescales are very different this is a non-trivial exercise and mature edge codes typically require preconstructed field-aligned grids, which makes following the continuous plasma shape and current profile evolution extremely challenging. An alternative approach, adopted here, is to use a database of stationary edge plasma solutions to derive a set of boundary conditions that could be supplied to the codes capable of full scenario simulations. An initial database of limiter plasma simulations was constituted using the SOLPS-ITER code package, including the release and transport of all W ion charge states up to a given cut-off, as part of the re-baseline activities

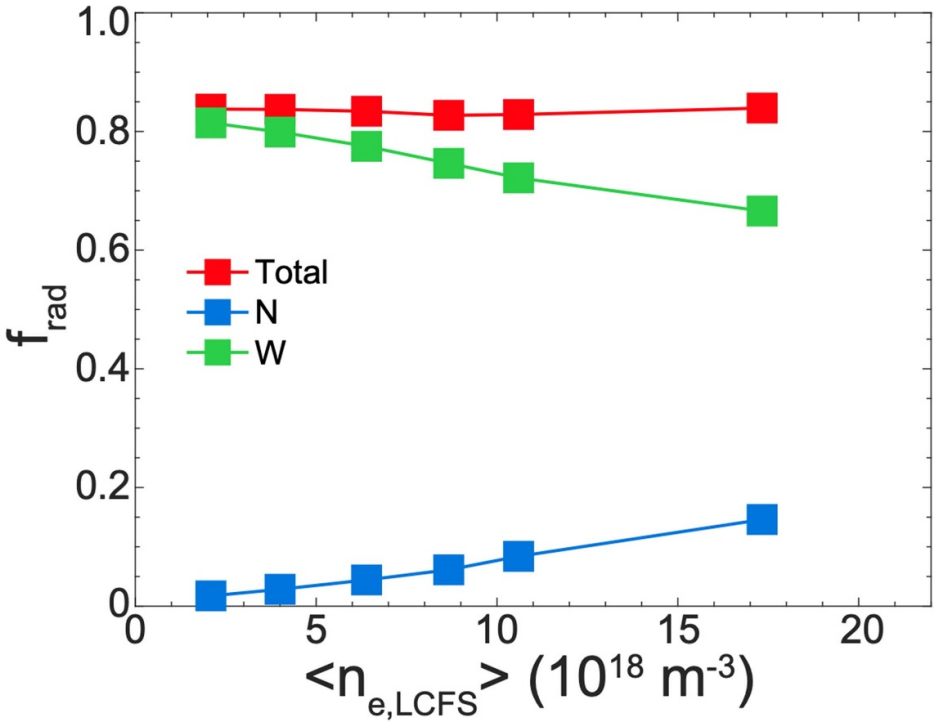

Figure 16. Total fraction of P_{heat} radiated inside the core (in red) and individual contributions from N (in blue) and W (in green) as functions of electron density at the LCFS obtained in simulations with the 0.5% N concentration and 'prompt redeposition' included.

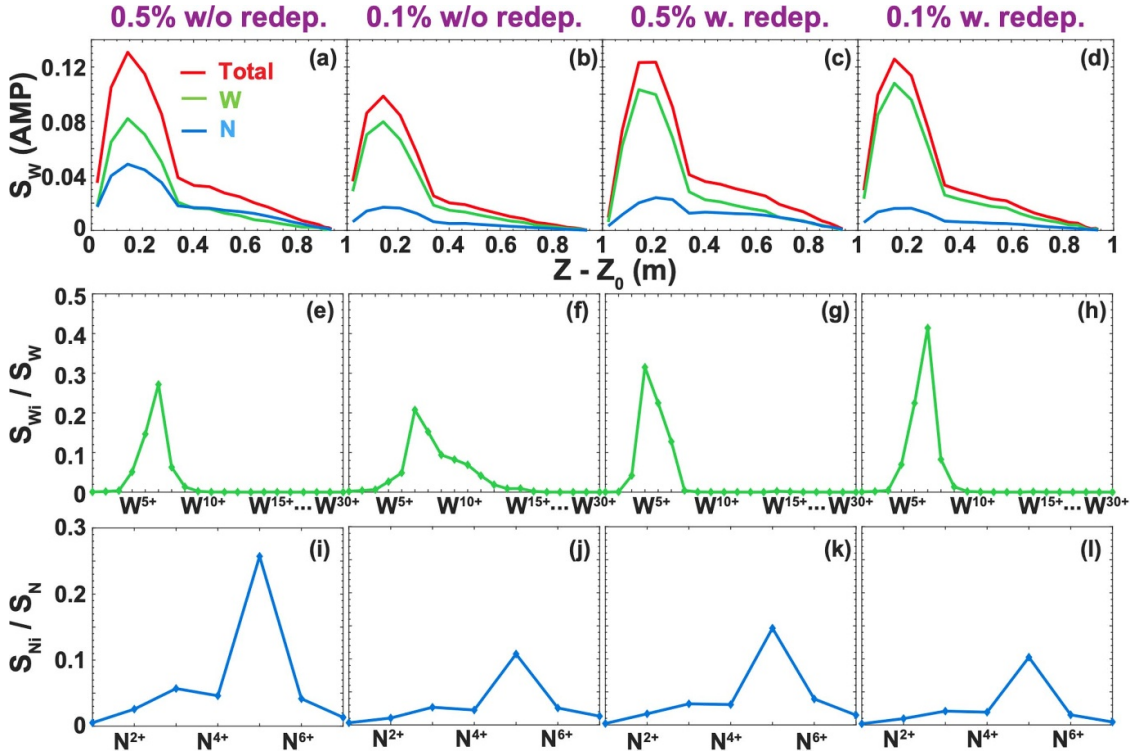

Figure 17. Erosion contributions from different components in 4 cases (marked in figure 15(*a*)) corresponding to different N concentration with and without 'prompt redeposition' at $<n_{e,LCFS}> \sim 5 \times 10^{18}$ m^{-3}. Top row: profiles of W erosion by W ions (in green), N ions (in blue), W and N combined (in red) along the limiter surface. Middle row: relative contribution of different W charge states to the erosion. Bottom row: relative contribution of different N charge states to the erosion.

(described in [1]). Analysis of the database provided a simple relationship between the equilibrium plasma temperature and density at the LCFS (see equation (3)) which was used to construct the boundary condition for the DINA code, one of the main tools deployed for end-to-end ITER scenario simulations including magnetic control [1]. This paper has reported on findings from a significant expansion of the database designed to explore several additional numerical aspects and physics elements which were ignored in the initial simulations in order to provide rapid early conclusions in support of the re-baselining.

Results derived from the new database show that the SOL plasma solution is insensitive to both the extension of the computational grid into the SOL beyond 10 cm (at the OMP) and the core plasma heating profile. The simulations also confirm that the profiles of W self-sputtering and W sputtering by residual/seeded impurities are alike. This was the assumption which permitted the approach in [1] of employing the same correction factor for the W limiter sputtering due to all ions leaving the LCFS [1]. The validity of two of the main assumptions used in [1] to justify the construction of DINA limiter phase LCFS boundary conditions is therefore confirmed by the expanded SOLPS-ITER database. It is nevertheless the case that regression in the larger database indicates that the fit for $<T_{\mathrm{e,LCFS}}>(<n_{\mathrm{e,LCFS}}>)$ used to formulate the boundary conditions (i.e. equation (3) should be improved by incorporating the dependence on P_{heat}, which turns out to make a contribution of the same order of importance as that of $<n_{\mathrm{e,LCFS}}>$ (see equations (4)–(6). Moreover, the resulting expression depends on the SOL plasma transport assumptions. To address the possible impact, a SOL plasma transport scan was conducted over a broad range of λ_q from 4 mm to almost 5 cm, corresponding to near and far λ_q scales predicted by the scaling in [13] used to define the ITER inner FW panel toroidal shaping. It was found that an order of magnitude variation in λ_q translates to a ∼30% variation of $<T_{\mathrm{e,LCFS}}>$ at given $<n_{\mathrm{e,LCFS}}>$ in the medium density range (the difference is higher at extremely low densities but these are unlikely to be very relevant to the ITER current ramp-up plasmas which aim more at $<n_{\mathrm{e}}>/n_{\mathrm{GW}} \sim 0.5$ [6]).

Another important physics uncertainty, missing from the treatment in [1], is the influence of the prompt redeposition. The promptly redeposited fraction of W eroded from the limiter surface has been estimated here by the ERO code to be in the range of 25% to 45% (increasing with the SOL plasma density) for typical SOL plasma solutions obtained with SOLPS-ITER. Its impact on the SOL plasma solution is assessed in a simplified way by means of a simple correction to the W physical sputtering yield (corresponding to an averaged prompt redeposition of 35%) in a series of SOLPS-ITER simulations. For given $<n_{\mathrm{e,LCFS}}>$, accounting for prompt redeposition in in this approximative way raises $<T_{\mathrm{e,LCFS}}>$ by almost a factor of 1.5 compared to the cases without prompt redeposition. Moreover, in this case, the sputtering by H ions becomes non-negligible, indicating that a further increase in prompt redeposition (or a transition from H to D) would result in a change of attractor of the system from $<Y_{\mathrm{W\text{-}W}}> = 1$ to $<Y_{\mathrm{W\text{-}W}}> + <Y_{\mathrm{H,D\text{-}W}}> \times \Gamma_{\mathrm{H,D}}/\Gamma_{\mathrm{W}} = 1$.

Finally, feedback-controlled nitrogen injection was introduced in the simulations as a proxy for the inevitable impurities which will be present in the start-up plasma of any real tokamak (in particular oxygen, one of the most common and difficult impurities in the start-up plasma and which has very similar ionization potentials and cooling functions to those of N). It was found that with N-seeding the system is attracted to $<Y_{\mathrm{W\text{-}W}}> + <Y_{\mathrm{imp\text{-}W}}> \times \Gamma_{\mathrm{imp}}/\Gamma_{\mathrm{W}} = 1$ rather than $<Y_{\mathrm{W\text{-}W}}> = 1$, resulting in typical LCFS temperatures of ∼20 eV instead of ∼(40–50) eV for pure H plasmas. Unlike in unseeded simulations, a moderate N content (fixed to 0.1% of the H content at $<n_{\mathrm{e,LCFS}}>/n_{\mathrm{GW}} = 0.15$) is enough to maintain f_{rad} virtually saturated at ∼0.8 independently of $<n_{\mathrm{e,LCFS}}>$. Changes in $<n_{\mathrm{e,LCFS}}>$ result instead in redistribution of the radiated power between W and N ($f_{\mathrm{rad,N}}/f_{\mathrm{rad,W}}$ increases with raising density).

The more refined analysis reported in this paper shows that to improve equation (3) and make better quantitative predictions for the ITER current ramp-up phase, SOLPS-ITER should be furnished with a model allowing prompt redeposition to be treated self-consistently and locally. Understanding of the SOL plasma transport in the limiter phase should also be improved, especially for these ITER start-up plasmas at very high q_{LCFS} in which the SOL connection length can reach hundreds of meters. Even with these physics improvements in the model, the impurity content will remain the most important unknown that cannot be predicted in advance.

Despite the uncertainties, several clear conclusions can be drawn from this modelling exercise for ITER. It indicates that the plasma-limiter system by itself is inherently stable due to its self-regulation mechanism. As a consequence, with sufficient central EC heating to avoid W core accumulation and hollow temperature profiles, the limiter phase should not be overly problematic with a W FW. Issues arise from the steep early increase in heating power allowing for temporary W influx above the equilibrium value that would result in cooling of the plasma edge such that the residual impurities take over as the main radiators and drive the cold front inwards, triggering an MHD instability. Therefore, not only will sufficient central EC heating be required, but heating waveforms will have to be carefully tailored at this stage.

Possibly an even more important conclusion is that the heat flux to the FW will be limited by the equilibrium P_{LCFS} no matter the level of P_{heat}. The peak power loads originally estimated for the Be FW assuming negligible radiation losses will only be reached for a short period of time before the corresponding increase in P_{rad} due to the W influx will force them down. For the wide range of simulated plasma conditions encompassed in the expanded database, this equilibrium P_{LCFS} remains below ∼1 MW and, in the presence of the inevitable low Z impurities present in the early phase of any tokamak discharge, it tends to be at its lowest. Typical radiated fractions are in the range 0.6–0.8, increasing with P_{heat} since the equilibrium $P_{\mathrm{LCFS}} = P_{\mathrm{heat}} - P_{\mathrm{rad}}$. This result, if supported

by experimental evidence from current devices, indicates that the constraints imposed on the FW in ITER, particularly with regard to the stringent requirements on longwave alignment of the central column FW panels [3], might be somewhat relaxed as a consequence of the switch to W main chamber armor.

To ensure the validity of the model presented in this paper, it must first be validated against experiments conducted on present-day devices. As an initial step, dedicated limiter start-up experiments were performed at EAST [1], yielding favorable results that confirmed stable plasmas in contact with the W limiter over several seconds while maintaining a virtually constant $f_{\mathrm{rad}} \approx 0.6$. However, the diagnostics dataset for these shots was insufficient to fully constrain the code and achieve robust validation. Consequently, additional dedicated W experiments were conducted at ASDEX Upgrade and WEST to obtain a more comprehensive diagnostic dataset and further investigate quasi steady-state plasmas in contact with the W limiter. At present, these datasets have been gathered, and the modeling effort is underway to refine and validate the findings.

Acknowledgment

This work was supported by the National Natural Science Foundation of China under Grant No. 12235002, National MCF energy R&D Program No. 2024YFE03160000. The views and opinions expressed herein do not necessarily reflect those of the ITER Organization.

Appendix A

Here we summarize some practical recommendations specifically for SOLPS-ITER users working with similar W limiter plasma simulations to those described in this paper.

The following key ingredients are required to obtain physically meaningful solutions:

- The computational grid must be sufficiently extended into the core. Otherwise, the W content which self-regulates to provide the required $P_{\mathrm{LCFS}} = P_{\mathrm{heat}} - P_{\mathrm{rad}}$ will be unrealistically high. A practical recommendation is to grid as close to the magnetic axis as possible.
- If the grid extends deep into the confined region, it is important to suppress the artificial source from the minimal density imposed on the individual species (including fluid neutrals) for reasons of numerical stability. This source is normally negligible, but due to the large volume of the confined region if the grid is extended deep into the core and the extremely small W concentrations there, with the standard code settings this artificial source is high enough to provide for an unphysical accumulation of W in the center and even produce hollow temperature profiles. In our case, setting **'b2mndr_na_min'** to $\mathbf{1.0 \times 10^{3}}$ was sufficient to suppress this effect.
- To avoid unphysical excessive erosion of the W surface via self-sputtering, the boundary condition at the sheath interface should be set to $\geqslant c_{\mathrm{s}}$ for each individual species. This is achieved by setting the corresponding **'mompar(., ., 2)' > 0.5** (for example to 1.0) in the **b2.boundary.parameters** input file. The default boundary condition (corresponding to **'mompar(., ., 2)' < 0.5**) assumes that all the species are perfectly coupled to one another and arrive to the sheath entrance at the common sound speed of the system. This is not true for the W ions causing the most sputtering (typically charge states $\sim$ (+4–+8)) over the range of plasma densities envisioned for the limiter phase and will lead to a very large overestimate of the erosion source.
- For a crude estimate of the 'prompt redeposition' effect the **RECYCS** parameter can be changed for the corresponding surfaces in block 6 of the EIRENE input file. An example setting it to 0.65 is given below (with the corresponding parameter marked in bold):

SURFMOD_1_TUNGSTEN_SPT_1160K
1 2 −1 0 1 0
$1.84740 \times 10^{+4}$ -1.00000×10^{-1} 0.00000×10^{0} 0.00000×10^{0} 0.00000×10^{0} -1.00000×10^{0}
1.00000×10^{0} 1.00000×10^{0} 1.00000×10^{0} 1.00000×10^{0} 5.00000×10^{-1} 1.00000×10^{0}
0.65000×10^{0} 0.00000×10^{0} 0.00000×10^{0} 0.00000×10^{0} 1.00000×10^{0} 0.00000×10^{0}.

To obtain comparable solutions (for various parameter scans) in a reasonable computational time, the following techniques were found useful:

- Increase the time-step inside the confined region, where timescales are much larger, by a factor in **b2.numerics.parameters**. In our case the timestep for the SOL was usually set to 5.0×10^{-6} and it was increased by a factor $\sim$200 in the confined region. Alternatively, the 'method of effective sources' [40] or even a combination of both may be used.
- Establish a feedback control on the total content of the main ion species inside the confined region. This allows solutions to be obtained with approximately the same n_{LCFS} for different sets of input parameters without manually tweaking the gas puff. To achieve this, we recommend using the

'na_feedback_choice = 5' and specifying the rectangular section of the grid where feedback is applied to match the confined region in **b2.feedback_control.parameters**. This works well in conjunction with **'na_feedback_option = 4'**. On the first run the feedback target value must be tweaked manually until a reasonable plasma density is obtained. This value can be subsequently gradually changed (typically by 10%) in the desired direction (increasing or decreasing the density). Using the same set of feedback target values for two series of SOLPS-ITER simulations ensures that the average core plasma density will be the same. Moreover, if the core plasma transport is unchanged this also ensures that similar $<n_{e,LCFS}>$ values will be obtained for the two series of simulations.

- It is important to stress that all the speed-up schemes should be turned off when the quasi-steady state is reached, and simulations should be continued without them to ensure that the speed-up does not affect the stationary state.

Appendix B

This appendix provides a detailed description and systematic organization of the numerical cases utilized in this work. All 214 cases that appear in the figures are written to the public database, using the ITER Integrated Modeling and Analysis Suite (IMAS) Interface Data Structures (IDS) format [41]. Each simulation is assigned with unique shot number. Shot numbers corresponding to the simulations with specific setup, including transport coefficients, power input levels, and applied truncation strategies etc, are combined into series. To ensure clarity, shot numbers were assigned sequentially, and redundancies were avoided where applicable.

B.1. Double λ_q high series

Description:

The double exponential λ_q (double λ_q) cases with high SOL transport coefficients explore varying input power levels of 2.2 MW, 3.3 MW, and 4.4 MW. Each case is indexed from 1 to 10 according to the average electron density at the LCFS.

Shot Numbers: 106500–106529

Case Labels: fig3_double_lq_high_[2_2,3_3,4_4]MW_[1-10]_index

Note: These cases are identical to fig9_double_lq_high_[2_2,3_3,4_4]MW_[1-10]_index.

B.2. Double λ_q high SOL width and EC profile effects

To study the influence of SOL width and energy deposition profiles, the following sub-series were conducted:

B.2.1. SOL width effects

Description: tests SOL widths of 10 cm, 20 cm, and 33 cm at 2.2 MW input power.

Shot Numbers: 106530–106532

Case Labels: fig5_double_lq_high_[2_2]MW_[10,20,33]cm_sol_width

B.2.2. Broad EC profile with W^{30+} truncation

Description: simulation with broad EC profile and tungsten ion truncation up to W^{30+}.

Shot Numbers: 106533–106537

Case Labels: fig5_double_lq_high_[2_2]MW_broad_w30_[1-5]_index

B.2.3. Central EC profile with W^{47+} truncation

Description: simulation with central EC profile and W ion truncation up to W^{47+}.

Shot Numbers: 106538–106542

Case Labels: fig5_double_lq_high_[2_2]MW_central_w47_[1-5]_index

B.3. Double λ_q low series

Description: the double λ_q low series is subdivided into low, mid, and high levels of SOL transport coefficients. All cases share a similar near SOL decay length (∼4 mm), consistent with the choice in [3]. Simulations were performed for 2.2 MW, 3.3 MW, 4.4 MW, and 5.5 MW input power, with indices ranging from 1 to 5.

Shot Numbers: 106543–106602

Case Labels: fig9_double_lq_low_[low,mid,high]_sol_[2_2,3_3,4_4,5_5]MW_[1-5]_index

B.4. Double λ_q mid series

Description: the double λ_q mid series investigates SOL transport at mid-level for 2.2 MW, 3.3 MW, and 4.4 MW input power, with indices ranging from 1 to 8.

Shot Numbers: 106603–106626

Case Labels: fig9_double_lq_mid_[2_2,3_3,4_4]MW_[1-8]_index

B.5. Single λ_q series

Description: The single λ_q series explores **low, mid, and high SOL transport coefficients**:

B.5.1. Low transport coefficient

Shot Numbers: 106627–106631

Case Labels: fig9_single_lq_low_[2_2]MW_[1-5]_index

B.5.2. Mid transport coefficient

Shot Numbers: 106632–106646

Case Labels: fig9_single_lq_mid_[2_2,3_3,4_4]MW_[1-5]_index

B.5.3. High transport coefficient

Shot Numbers: 106647–106651

Case Labels: fig9_single_lq_high_[2_2]MW_[1-5]_index

B.6. Double high with prompt redeposition

Description: this series includes prompt redeposition of W ions (35%), with input power levels of **2.2 MW, 3.3 MW, and 4.4 MW** and indices **1–10**.

Shot Numbers: 106652–106681

Case Labels: fig13_double_lq_high_redeposition_[2_2,3_3, 4_4]MW_[1-10]_index

B.7. Single λ_q high series

Description: the single λ_q cases with **high SOL transport coefficients** explore input power levels **2.2 MW, 3.3 MW, and 4.4 MW**, with indices **1–5**.

Shot Numbers: 106682–106696

Case Labels: fig13_single_lq_high_[2_2,3_3,4_4]MW_[1-5]_index

B.8. Single mid HWN series

Description: this series includes hydrogen (H), tungsten ions (up to W^{30+}), and nitrogen (N^{+}-N^{7+}), with core N concentrations of **0.1% (01 N)** and **0.5% (05 N)**. Additional cases include prompt redeposition (35%).

B.8.1. HWN with 0.1% core N

Shot Numbers: 106697–106700

Case Labels: fig15_single_lq_mid_HWN_[2_2]MW_01N_[1-4]_index

B.8.2. HWN with 0.5% core N

Shot Numbers: 106701–106703

Case Labels: fig15_single_lq_mid_HWN_[2_2]MW_05N_[1-3]_index

B.8.3. HWN with 0.1% core N and redeposition

Shot Numbers: 106704–106708

Case Labels: fig15_single_lq_mid_redeposition_HWN_[2_2]MW_01N_[1-5]_index

B.8.4. HWN with 0.5% core N and redeposition

Shot Numbers: 106709–106714

Case Labels: fig15_single_lq_mid_redeposition_HWN_[2_2]MW_05N_[1-6]_index

B.9. Summary of shot numbers

Series	No. of cases	IDS shot numbers
Fig3_double_lq_high	30	106500–106529
Fig5_double_lq_high_sol_width	3	106530–106532
Fig5_double_lq_high_broad/central	10	106533–106542
Fig9_double_lq_low	60	106543–106602
Fig9_double_lq_mid	24	106603–106626
Fig9_single_lq_low/mid/high	25	106627–106651
Fig13_double_lq_high_redeposition	30	106652–106681
Fig13_single_lq_high	15	106682–106696
Fig15_single_lq_mid_HWN	18	106697–106714

ORCID iDs

Y. Zhang https://orcid.org/0000-0002-5188-0576
R.A. Pitts https://orcid.org/0000-0001-9455-2698
A. Kirschner https://orcid.org/0000-0002-3213-3225
C. Baumann https://orcid.org/0000-0001-7712-5379
S. Brezinsek https://orcid.org/0000-0002-7213-3326
J. Romazanov https://orcid.org/0000-0001-9439-786X
Chaofeng Sang https://orcid.org/0000-0002-6861-5242
Dezhen Wang https://orcid.org/0000-0003-0517-7318

References

[1] Pitts R.A. *et al* 2025 Plasma-wall interaction impact of the ITER re-baseline *Nucl. Mater. Energy* **42** 101854
[2] Loarte A. n.d. The new ITER baseline, research plan and open R&D issues *Plasma Phys. Control. Fusion* submitted
[3] Pitts R.A. *et al* 2022 First wall power flux management during plasma current ramp-up on ITER *Nucl. Fusion* **62** 096022
[4] Wiesen S. *et al* 2015 The new SOLPS-ITER code package *J. Nucl. Mater.* **463** 480–4
[5] Khayrutdinov R.R. and Lukash V.E. 1993 Studies of plasma equilibrium and transport in a tokamak fusion device with the inverse-variable technique *J. Comput. Phys.* **109** 193–201
[6] Gribov Y., Kavin A.A., Lukash V.E., Khayrutdinov R.R, Dubrov M., Pitts R.A., Pshenov A. and Schneider M. 2024 DINA simulations of ITER 15 MA hydrogen L-mode scenarios with tungsten first wall *50th EPS Conf. on Plasma Physics* (*Salamanca, 8–12 July 2024*) P4.090 (available at: https://lac913.epfl.ch/epsppd3/2024/html/PDF/P4-090.pdf)
[7] Stangeby P.C. 2000 *The Plasma Boundary of Magnetic Fusion Devices* (Institute of Physics Publishing)
[8] Post D.E., Jensen R.V., Tarter C.B., Grasberger W.H. and Lokke W.A. 1977 Steady-state radiative cooling rates for low-density, high-temperature plasmas *At. Data Nucl. Data Tables* **20** 397–439
[9] Schmid K., Mayer M., Adelhelm C., Balden M. and Lindig S. 2010 Impact of gyro-motion and sheath acceleration on the flux distribution on rough surfaces *Nucl. Fusion* **50** 105004
[10] García-Rosales C., Eckstein W. and Roth J. 1995 Revised formulae for sputtering data *J. Nucl. Mater.* **218** 8–17
[11] Eckstein W., Garcia-Rosales C., Roth J. and Ottenberger W. 1993 Sputtering data vol 9 p 352 (available at: http://cds.cern.ch/record/832227)
[12] Eckstein W. 2008 Sputtering yields *Vacuum* **82** 930–4
[13] Kocan M. *et al* 2015 Impact of a narrow limiter SOL heat flux channel on the ITER first wall panel shaping *Nucl. Fusion* **55** 033019
[14] Fussmann G., Engelhardt W. and Naujoks D. 1995 *High-Z Elements as Target Materials in Fusion Devices, IAEA* (International Atomic Energy Agency (IAEA))
[15] Kirschner A., Philipps V., Winter J. and Kogler U. 2000 Simulation of the plasma—wall interaction in a tokamak with the Monte Carlo code ERO-TEXTOR *Nucl. Fusion* **40** 989–1001
[16] Maget P. *et al* 2022 Healing plasma current ramp-up by nitrogen seeding in the full tungsten environment of WEST *Plasma Phys. Control. Fusion* **64** 045016
[17] Braams B.J. 1986 Computational studies in tokamak equilibrium and transport *PhD thesis* Rijksuniversiteit, Utrecht, Nederlands (available at: https://inis.iaea.org/search/search.aspx?orig_q=RN:18038616) (Accessed 28 August 2017)
[18] Reiter D., Baelmans M. and Börner P. 2005 The EIRENE and B2-EIRENE Codes *Fusion Sci. Technol.* **47** 172–86
[19] Pshenov A.A., Kukushkin A.S. and Krasheninnikov S.I. 2017 On detachment asymmetry and stability *Phys. Plasmas* **24** 072508
[20] Eckstein W. 2002 *Calculated Sputtering, Reflection and Range Values* (Garching)

[21] Tskhakaya D. 2017 One-dimensional plasma sheath model in front of the divertor plates *Plasma Phys. Control. Fusion* **59** 114001
[22] Lee D., Oksuz L. and Hershkowitz N. 2007 Exact solution for the generalized Bohm criterion in a two-ion-species plasma *Phys. Rev. Lett.* **99** 155004
[23] Baalrud S.D. and Hegna C.C. 2011 Determining the Bohm criterion in plasmas with two ion species *Phys. Plasmas* **18** 023505
[24] Bucalossi J. *et al* 2024 WEST full tungsten operation with an ITER grade divertor *Nucl. Fusion* **64** 112022
[25] Neu R. *et al* 2009 Ten years of W programme in ASDEX Upgrade—challenges and conclusions *Phys. Scr.* **T138** 014038
[26] de Vries P.C. and Gribov Y. 2019 ITER breakdown and plasma initiation revisited *Nucl. Fusion* **59** 096043
[27] Moro A. *et al* 2017 Electron cyclotron stray radiation detection and machine protection system proposal for JT-60SA *Fusion Eng. Des.* **123** 435–9
[28] Greenwald M. 2002 Density limits in toroidal plasmas *Plasma Phys. Control. Fusion* **44** R27–R53
[29] Marenkov E.D., Pshenov A.A. and Kukushkin A.S. 2022 Simulation of lithium flow, redeposition, and vapor shielding in liquid lithium divertor of T-15MD tokamak with SOLPS 4.3 code *Plasma Phys. Control. Fusion* **64** 115006
[30] Nallo G.F., Mazzitelli G., Moscheni M., Subba F. and Zanino R. 2022 SOLPS-ITER simulations of a CPS-based liquid metal divertor for the EU DEMO: Li vs Sn *Nucl. Fusion* **62** 036008
[31] Marenkov E.D. 2024 The kinetic theory of prompt redeposition in the case of thin Debye sheath *Phys. Plasmas* **31** 053512
[32] Tskhakaya D. and Groth M. 2015 Modelling of tungsten re-deposition coefficient *J. Nucl. Mater.* **463** 624–8
[33] Guterl J., Bykov I., Ding R. and Snyder P. 2021 On the prediction and monitoring of tungsten prompt redeposition in tokamak divertors *Nucl. Mater. Energy* **27** 100948
[34] Brooks J.N. 1990 Near-surface sputtered particle transport for an oblique incidence magnetic field plasma *Phys. Fluids B* **2** 1858–63
[35] Kirschner A., Tskhakaya D., Brezinsek S., Borodin D., Romazanov J., Ding R., Eksaeva A. and Linsmeier C. 2018 Modelling of plasma-wall interaction and impurity transport in fusion devices and prompt deposition of tungsten as application *Plasma Phys. Control. Fusion* **60** 014041
[36] Summers H.P. 2004 The ADAS User Manual, version 2.6
[37] Eckstein W., Dohmen R., Mutzke A. and Schneider R. 2007 SDTrimSP: a Monte-Carlo code for calculating collision phenomena in randomized targets *Report IPP 12/3*
[38] Coster D.P., Bonnin X., Mutzke A., Schneider R. and Warrier M. 2007 Integrated modelling of the edge plasma and plasma facing components *J. Nucl. Mater.* **363–365** 136–9
[39] Wauters T., Hagelaar G.J.M. and Pitts R.A. 2025 Modeling input to the ITER glow discharge boronization system design *Nucl. Mater. Energy* **42** 101891
[40] Kaveeva E., Rozhansky V., Senichenkov I., Veselova I., Voskoboynikov S., Sytova E., Bonnin X. and Coster D. 2018 Speed-up of SOLPS-ITER code for tokamak edge modeling *Nucl. Fusion* **58** 126018
[41] Imbeaux F. *et al* 2015 Design and first applications of the ITER integrated modelling & analysis suite *Nucl. Fusion* **55** 123006